Check for updates

ASCE

Performance of Ordinary C-Shaped Reinforced Concrete Structural Walls Subjected to Wind Loading Protocols

Mehmet Emre Unal, Ph.D.[1]; Eric Ahlberg, Ph.D., P.E.[2]; Kevin Aswegan, P.E., S.E., M.ASCE[3]; Juliana Rochester, P.E., S.E., M.ASCE[4]; Ron Klemencic, P.E., S.E., Dist.M.ASCE[5]; and John W. Wallace, Ph.D., P.E., F.ASCE[6]

Abstract: Building design in ASCE/SEI 7 for extreme wind loads is based on elastic behavior, which eliminates the need to develop special detailing and capacity design rules to account for nonlinear responses. Recently, ASCE published a *Prestandard for Performance-Based Wind Design* that would allow modest nonlinear responses under wind loading to reduce construction costs while maintaining equivalent structural performance and safety, and address unintended negative impacts of wind design on buildings that are located in areas with both extreme wind and seismic hazards. Wind forces tend to have the greatest impact on taller buildings, where it has become common to utilize reinforced concrete core walls to resist lateral wind and seismic forces. Therefore, a study was conducted to investigate the performance of four large-scale reinforced concrete walls with C-shaped cross sections subjected to a biaxial wind loading protocol (WLP) followed by a seismic loading protocol (SLP). Prior to the wall testing, beam testing was conducted under WLPs to develop design requirements for lap splice lengths above the wall–foundation interface. The wall test results indicate that current ACI 318-25 detailing requirements are adequate for the wall with longitudinal reinforcement ratio (ρ_l) of 0.75%, which completed the WLP without noticeable damage or strength loss; however, for the walls with ρ_l of 1.5%, additional detailing at flanges edges may be needed to limit damage due to concrete crushing and longitudinal bar buckling, depending on the level of axial stress induced at the flange edges under biaxial loading. Based on the test results, strain acceptance criteria are recommended. **DOI: 10.1061/JSENDH.STENG-15220.** © *2025 American Society of Civil Engineers.*

Author keywords: Performance-based wind design; Reinforced concrete; Wind loading; Structural wall.

Introduction

Although improvements have been made to characterize wind demands over the last few decades, ASCE 7 (ASCE 2022) still requires buildings to be designed to remain essentially elastic during extreme wind events. ASCE/SEI 7 and the material codes [e.g., American Concrete Institute (ACI) standard ACI 318] do not provide acceptance criteria under wind loading for drift or occupant comfort because these criteria are serviceability-related versus life safety–related (Klemencic et al. 2019). Unlike for wind design, performance-based seismic design (PBSD) guidelines with both service-level and collapse prevention [risk-targeted maximum considered earthquake (MCE$_R$)] acceptance criteria have been used for more than 20 years [LATBSDC 2005; FEMA 273 (FEMA 1997)]. For PBSD, the limited yielding permitted for service-level demands and the potentially significant yielding permitted for MCE$_R$ demands are accommodated by requiring special detailing to allow yielding without strength loss for ductile component actions and using capacity design or amplified forces for component actions that are brittle or have limited ductility. The special detailing requirements used for PBSD are primarily based on ACI 318 provisions (for reinforced concrete), which are based on a long history of postearthquake performance assessment and a large number of laboratory tests.

Building design based on essentially linear behavior under extreme wind demands, versus allowing for modest nonlinear behavior, very likely results in higher construction costs for wind design. In addition, for buildings that are located where both significant wind and seismic hazards exist, the wind design requirements can have a significant negative impact on the seismic design, e.g., if the elastic wind demands exceed the reduced seismic demands, the capacity-based seismic design checks are based on the strength required for the higher wind demands. Given the potential benefits of allowing limited nonlinear responses under extreme wind demands, ASCE developed a *Prestandard for Performance-Based Wind Design* (ASCE 2019) that provides modeling approaches, building performance objectives, and corresponding acceptance criteria. The goal of creating the Prestandard was to enable the design of more efficient and cost-effective buildings by allowing limited nonlinear behavior in specified component actions of the

[1]Product Engineer, Simpson Strong-Tie, 5956 W. Las Positas Blvd., Pleasanton, CA 94588 (corresponding author). ORCID: https://orcid.org/0000-0002-9768-9670. Email: umehmetemre@gmail.com

[2]Lecturer and Development Engineer, Dept. of Civil and Environmental Engineering, Univ. of California, Los Angeles, CA 90095. Email: eahlberg@ucla.edu

[3]Principal, Magnusson Klemencic Associates, 1301 5th Ave., Seattle, WA 98101. Email: kaswegan@mka.com

[4]Associate, Magnusson Klemencic Associates, 1301 5th Ave., Seattle, WA 98101. Email: jrochester@mka.com

[5]Chairman and CEO, Magnusson Klemencic Associates, 1301 5th Ave., Seattle, WA 98101. Email: rklemencic@mka.com

[6]Professor, Dept. of Civil and Environmental Engineering, Univ. of California, Los Angeles, CA 90095. Email: wallacej@ucla.edu

Note. This manuscript was submitted on March 19, 2025; approved on July 24, 2025; published online on October 25, 2025. Discussion period open until March 25, 2026; separate discussions must be submitted for individual papers. This paper is part of the ***Journal of Structural Engineering***, © ASCE, ISSN 0733-9445.

main wind force–resisting system (MWFRS) that meet prescribed performance objectives.

As mentioned previously, detailing and capacity design requirements for PBSD are based on significant prior research and observation. For example, thousands of large-scale laboratory tests under seismic loading protocols (SLPs) have been conducted to develop the design requirements incorporated into ACI 318-25. Although the knowledge obtained from the development and use of PBSD has helped in the development of performance-based wind design (PBWD), there are fundamental differences between seismic and wind loads and the response of buildings to these loads.

Some of these differences include (1) the duration of loading, i.e., typically less than 1–2 min for strong earthquakes, versus hours or days for strong wind events, (2) the number of cycles, i.e., typically limited to 25 or 30 cycles for strong earthquakes, versus hundreds or thousands of cycles for strong wind events, and (3) the differences between the along-wind (variation about a mean demand) and across-wind (zero mean) loading. As a result of these differences, testing of RC components is needed under wind loading protocols (WLPs) to develop design provisions for stable nonlinear response and to avoid brittle failures.

The application of PBWD will have the greatest impact on taller buildings, where core wall systems are typically used for the MWFRS. These core wall systems consist of various wall segment shapes (e.g., planar, C-, I-, or H-shaped) connected with coupling beams (link beams) at floor levels. Although limited, there are some published research studies that focused on the performance of large-scale reinforced concrete (Abdullah et al. 2020, 2021, 2022; Chou et al. 2023) and steel (Hill et al. 2023) coupling beams tested using WLPs. However, there are no published studies focused on the testing of structural walls under WLPs, and only limited test results are available for biaxial seismic loading protocols for flanged walls, likely due to the large loads required to test even modest-scale walls and the complexity of testing under biaxial lateral loading with axial load. Wind loading protocols are also challenging due to the large number of cycles that are applied.

This study addresses this knowledge gap by reporting test results on four C-shaped structural walls with either constant or variable axial stresses under biaxial WLPs. The objectives of the research program were to (1) develop a test program for isolated C-shaped wall tests that could adequately represent the demands on C-shaped walls as components of core walls of buildings designed and constructed in high-wind zones in the US, (2) assess the performance of ordinary walls, i.e., walls designed and detailed according to Chapter 11 of ACI 318 (ACI 2025), to determine if additional design requirements are needed to achieve acceptable performance for modest inelastic demands under WLPs, and (3) evaluate the reserve (residual) seismic capacity of walls subjected to prior wind loading protocols with limited nonlinear demands.

Experimental Program

Specimen Design

The test specimen designs were based on a review of tall buildings designed and built in high-wind and low-seismic regions of the US, including buildings located in Austin and Houston (Texas), Miami, and Chicago. Roof heights for these buildings ranged from 65.5 m (215 ft) to 160 m (525 ft), and the lateral force–resisting systems were reinforced concrete core walls comprised of C- and/or I-shaped walls connected with coupling beams. The geometry and reinforcement at wall critical sections (expected plastic hinge regions) for eleven C-shaped walls were reviewed to assess the ranges in the following parameters: thickness [$t = 305$ mm (12 in.) to 915 mm 36 in.)], length [$l = 2$ m (6.5 ft) to 10 m 32.5 ft.)], longitudinal reinforcement ratio ($\rho_l = 0.3\%$ to 2.8%), and transverse reinforcement ratio ($\rho_t = 0.2\%$ to 1.1%).

Based on input from a Project Advisory Committee (PAC) that included practicing structural engineers from four engineering firms involved in the wind design of tall RC core wall buildings, ρ_l was selected as the test variable for the Phase I test specimens (two walls). Given the range of ρ_l provided in the reviewed buildings, $\rho_l = 0.75\%$ and $\rho_l = 1.5\%$ were selected for the first (CW-1) and second (CW-2) test walls, respectively. Based on the results of the Phase I tests, Phase II consisted of two additional wall tests (CW-3 and CW-4) where the longitudinal reinforcement ratio was held constant at 1.5%, and the test variables included variation of axial load during out-of-plane loading and the level of detailing provided at the flange edges.

The thickness of the flanges (t_f) and webs (t_w) of all four test specimens was selected to be 127 mm (5 in.) based on ACI 318-25 requirements for minimum cover over longitudinal reinforcement and the capacity of the test setup. Flange and web lengths of 762 mm (30 in.) and 1,905 mm (75 in.) were selected based on test setup limitations to produce cross-sectional aspect ratios of 6 (l_f/t_f) and 15 (l_w/t_w), which were similar to the mean values observed in the reviewed buildings. The longitudinal (vertical) reinforcement consisted of No. 3 (Table 2) Grade 60 for CW-1 (Fig. 1) and No. 4 Grade 80 for CW-2, CW-3, and CW-4 (Fig. 2). Grade 80 reinforcement was used because its use is common in tall buildings; however, Grade 60 reinforcement was used for CW-1 because No. 3 Grade 80 reinforcement is not available in the US.

Because ASCE 7-22 requires components of building MWFRS to remain elastic under wind demands, the design of the structural walls is governed by the provisions of Chapter 11 of ACI 318-25 (ordinary walls). For core walls, it is common practice to distribute the longitudinal reinforcement uniformly rather than to concentrate longitudinal reinforcement at the wall edges, which is often done for special walls (walls designed according to Chapter 18 provisions of ACI 318-25). For the first two tests, based on common design practice, transverse reinforcement consisted of U-bars at wall edges and corners lapped with the flange and web horizontal reinforcement. For the Phase II walls, due to damage observed for CW-2 (concrete crushing and longitudinal bar buckling), hoops were provided at the flange edges (Fig. 3) based on a procedure similar to that developed by Wallace and Orakcal (2002), which is used in ACI 318-25 §18.10.6.2 for detailing the special boundary elements. According to Wallace and Orakcal (2002), the region of the wall (c'') over which closely spaced transverse reinforcement is required can be calculated as follows:

$$\frac{c''}{l_w} = \frac{c}{l_w} - \frac{1}{667(\delta_u/h_w)} \tag{1}$$

where c = neutral axis depth; δ_u = design displacement; and l_w and h_w = length and height of the wall. A value of $\delta_u/h_w = 0.015$ was assumed to develop the ACI 318-25 requirement (Wallace and Orakcal 2002) for seismic detailing of special walls; however, because the purpose of these tests is to investigate wall behavior under wind demands, the use of a smaller value is appropriate.

During the testing of CW-2, the plastic hinge yield rotation ($\theta_{y,\mathrm{CW2}}$) was estimated to be 0.003 ("Instrumentation" section and Fig. 7). Therefore, to reach $3\theta_y$ (maximum WLP hinge rotation demand for this test program is $3\theta_y = 0.009$, as mentioned in the "Wind Loading Protocol" section), the roof level drift (δ_u/h_w) was estimated to be 0.01 (assuming the contribution of elastic

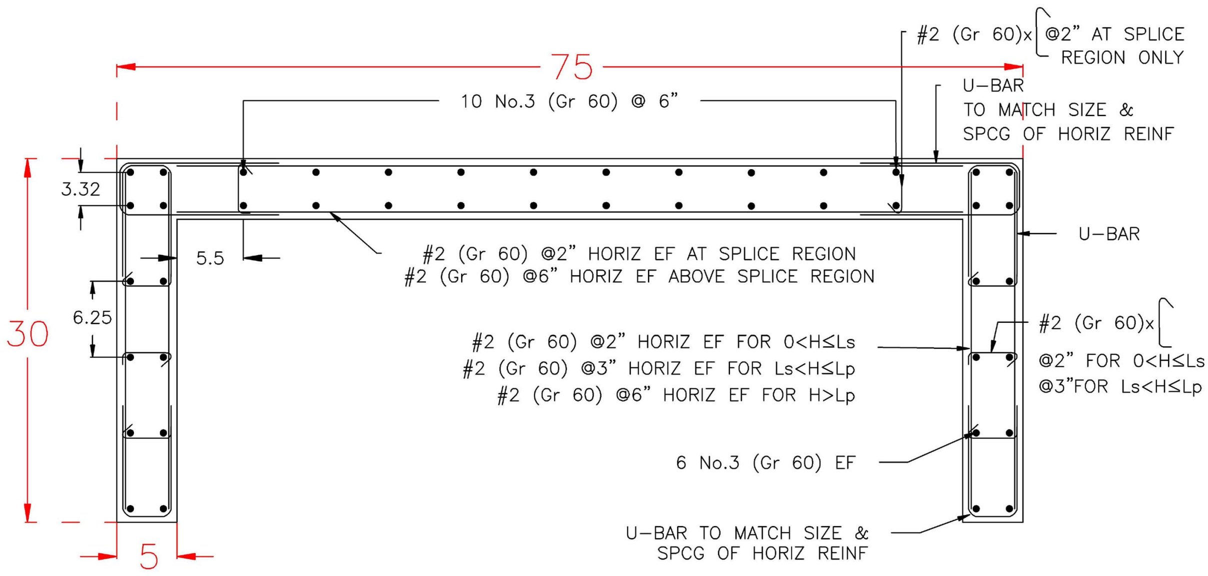

Fig. 1. Cross section and reinforcement of CW-1 (units are in inches, 1 in. = 25.4 mm).

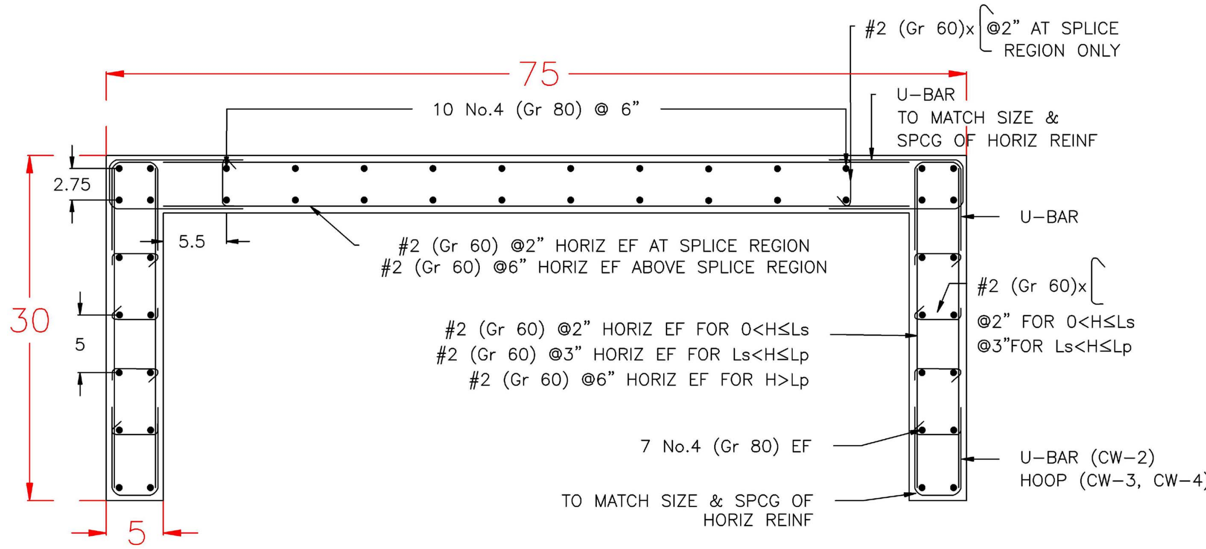

Fig. 2. Cross section and reinforcement of CW-2, CW-3, and CW-4 (units are in inches, 1 in. = 25.4 mm).

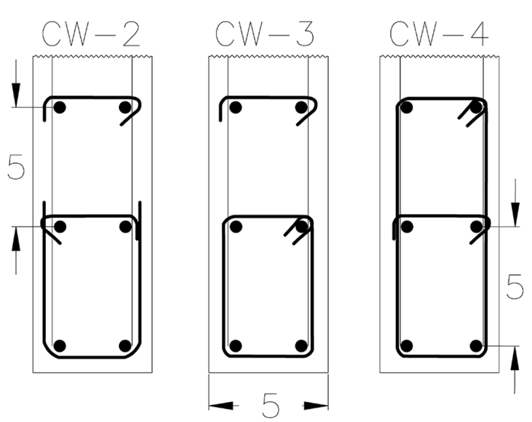

Fig. 3. Detailing of flange edges within plastic hinge region, $h < L_p$ (units are in inches, 1 in. = 25.4 mm).

deformations over the wall height to roof drift is small). Consequently, the wall length where confinement should be provided for the test specimens CW-3 and CW-4 was calculated as follows:

$$c'' = c - 0.15 l_w \tag{2}$$

For the calculation of c, the commercial software CSICol version 10 was used, and biaxial loading was applied with the maximum moment and axial load demands expected from the WLP developed for the C-wall testing ("Wind Loading Protocol" section).

Based on this procedure, for CW-3, a single hoop was used to confine the region between the first two layers of flange edge longitudinal (vertical) reinforcement. Similarly, a longer hoop that encloses the area between the first and the third layers of longitudinal (vertical) reinforcement, along with a seismic crosstie (135° hook at one end and 90°, one at the other, referred to as 135-90 crossties herein) for the second layer of reinforcement, was used for the flanges of CW-4 (Fig. 3). More information related to the approach

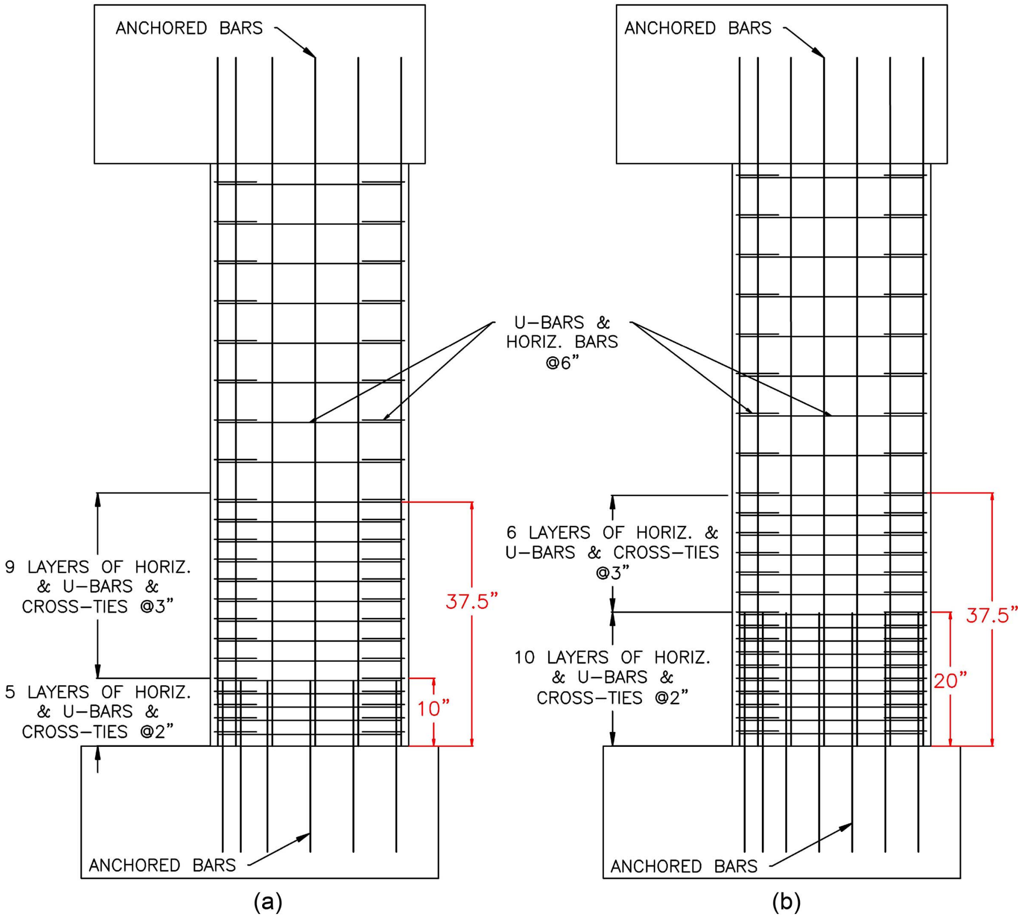

Fig. 4. Elevation of the flanges: (a) CW-1; and (b) CW-2 (units are in inches, 1 in. = 25.4 mm).

used to determine flange edge detailing has been given by Unal (2024). Although a roof level drift ratio of $\delta_u/h_w = 0.01$ was deemed appropriate for the Phase II test specimens despite being recognized as a larger roof drift than most tall buildings would experience, a similar analysis would be required to determine detailing requirements for other wall configurations.

To represent typical construction for ordinary walls, longitudinal reinforcement was lap-spliced at the wall–foundation interface (critical section) of the test walls; however, given the uncertainty associated with the lap splice behavior under the wind loading protocol, a separate study was conducted to determine splice design requirements prior to the construction of Phase I walls. This study included tests on RC beams under wind loading protocols with lap splices with the same reinforcement (longitudinal and transverse) diameter, grade, and clear cover as CW-2 (the specimen with the highest longitudinal strain demands expected at the critical section).

Based on a review of the beam test results (Unal et al. 2024; Halim 2024) and discussions with the PAC, the following design requirements were implemented. First, the lap splice lengths calculated for ordinary walls using ACI 318-25 Chapter 11 were multiplied by 1.25 [$l_s = 1.25\ (1.30 l_d)$], resulting in $l_s = 254$ mm (10 in.) for CW-1 and $l_s = 510$ mm (20 in.) for CW-2, CW-3, and CW-4 (Fig. 4). The 1.25 multiplier was applied to account for the expected yield strength ($f_{y,\mathrm{exp}}$) of the longitudinal reinforcement and the possibility of modest strain hardening; the same multiplier is applied in ACI 318-25 Section 18.10.2.3(b) for regions above the critical section of special walls (ACI 318-25 prohibits the use of lap splices at the critical section of special walls).

In addition, the lap splices were enclosed with 6-mm (d_b = 0.24 in.) Grade 500 (MPa) transverse reinforcement spaced at 51 mm (2 in.) along the splice length, as described in the following sentences. At the intersections of the flange and web, transverse reinforcement consisted of U-bars for both the Phase I and Phase II tests (Figs. 1 and 2). At the flange edges, U-bars were used for Phase I tests, and hoops were used for Phase II tests (Fig. 3). For longitudinal bars along the flange and for the first pair of web longitudinal bars adjacent to the flange–web corner, 135-90 crossties were provided (Figs. 1 and 2). No additional transverse reinforcement was provided for the remaining web longitudinal bars (Figs. 1 and 2).

The spacing (s) of transverse reinforcement above the splice ($h > l_s$) was determined using bar buckling models (Rodriguez et al. 1999; Moyer and Kowalsky 2003; Hilson et al. 2014; Rodriguez and Iñiguez 2019; Motter et al. 2018) to prevent longitudinal bar buckling prior to the completion of WLP. Based on Unal (2024), 6-mm Grade 500 (MPa) transverse reinforcement at a spacing of 76 mm (3 in.) (Fig. 4) was used to support longitudinal reinforcement within the flange and at flange–web corners between the top of the splice and the extent of the assumed plastic hinge region (i.e., $L_p > h > l_s$), where L_p was estimated as $L_p = l_w/2 =$ 0.95 m (37.5 in.).

In the wall flanges above the plastic hinge length ($h > L_p$) and in the web above the splice region ($h > l_s$), the spacing of the transverse reinforcement and the U-bars were based on spacing limits given in ACI 318-25 §11.7.3 for ordinary walls. According to §11.7.3, the spacing (s) of the transverse reinforcement in cast-in-place walls should not exceed the lesser of three times the wall thickness [38.1 cm (15 in.)], 45.7 cm (18 in.) [15.2 cm (6 in.)

Table 1. Tested properties of concrete on the specimen test day

Specimen	No. of samples	$f_{c,\text{test}}$ [MPa (psi)]	$\varepsilon_{@fc,\text{test}}$
CW-1	3	55.0 (7,976)	0.0032
CW-2	4	71.3 (10,340)	0.0030
CW-3	4	54.7 (7,932)	0.0030
CW-4	4	56.4 (8,177)	—

for the approximately 1/3 scaled test walls], and $l_w/5$ [190 cm/5 = 38 cm (15 in.)]; therefore, $s = 15.2$ cm (6 in.) was used (Fig. 4). More information regarding the design of the test specimens has been given by Unal (2024).

Material Properties

The concrete mix was designed to have a 28-day compressive strength (f'_c) of 55 MPa (8,000 psi) with a maximum aggregate size of 9.5 mm (3/8 in.). Results of concrete cylinders collected in accordance with ASTM C31/C31M (ASTM 2023a) and tested in accordance with ASTM C39/C39M (ASTM 2023b) are presented in Table 1. Properties of the No. 3 ASTM A706 (ASTM 2022) Grade 60 and No. 4 A706 Grade 80 deformed bars used for the longitudinal reinforcement and for the 6-mm Grade 500 (MPa) reinforcement used for web transverse reinforcement, U-bars, and crossties are provided in Table 2.

Test Setup and Instrumentation

The test setup (Fig. 5) was designed to apply both in-plane (IP) (parallel to the wall web, or x-direction) and out-of-plane (OOP) (parallel to the wall flanges, or y-direction) moment and shear demands at the top of the test specimen by using six actuators. Two vertical and a single horizontal actuator in the plane of the web were used to apply the in-plane moment and shear demands, whereas two horizontal actuators aligned perpendicular to the wall web were used to apply the OOP shear and OOP moment demands, and a third vertical actuator, connected to the top cap of the specimen using steel beams, was used to apply additional OOP moment demands. The vertical actuators, used in the IP and OOP directions to apply moment demands at the top of the walls (Fig. 5), were used to better simulate the boundary conditions in real structures, i.e., the test walls only represented the first two stories of a tall structure ("Wind Loading Protocol" section).

Table 2. Tested mechanical properties of reinforcement

Bar No. (diameter)	$f_{y,\text{test}}$ [MPa (ksi)]	ε_y	f_{peak} [MPa (ksi)]	f_{rup} [MPa (ksi)]	ε_{rup}
6 mm	473.7 (68.7)	0.0024	527.5 (76.5)	406.1 (58.9)	0.07
No. 3 [9.5 mm (0.375 in.)]	494.4 (71.7)	0.0025	710.2 (103)	570.2 (82.7)	0.13
No. 4 [12.7 mm (0.5 in.)]	584.7 (84.8)	0.0029	759.1 (110.1)	547.4 (79.4)	0.15

Note: Average values of four samples are presented.

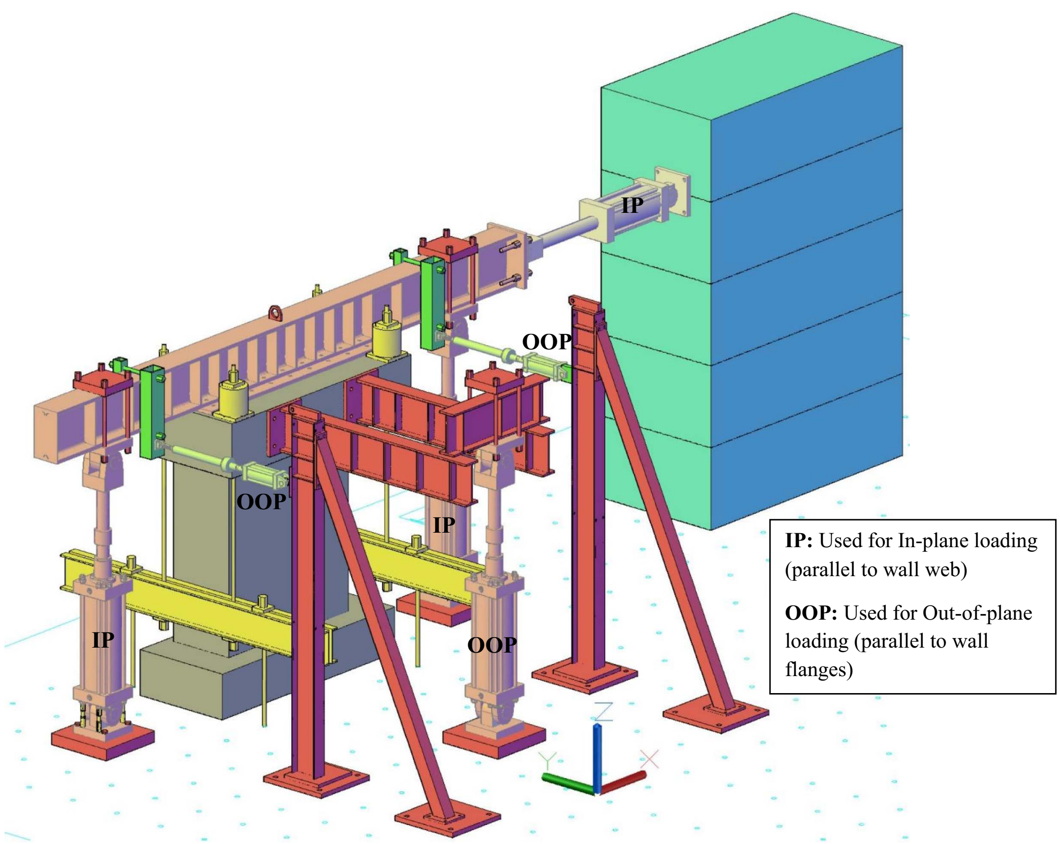

Fig. 5. Isometric view of the test setup (not drawn to scale).

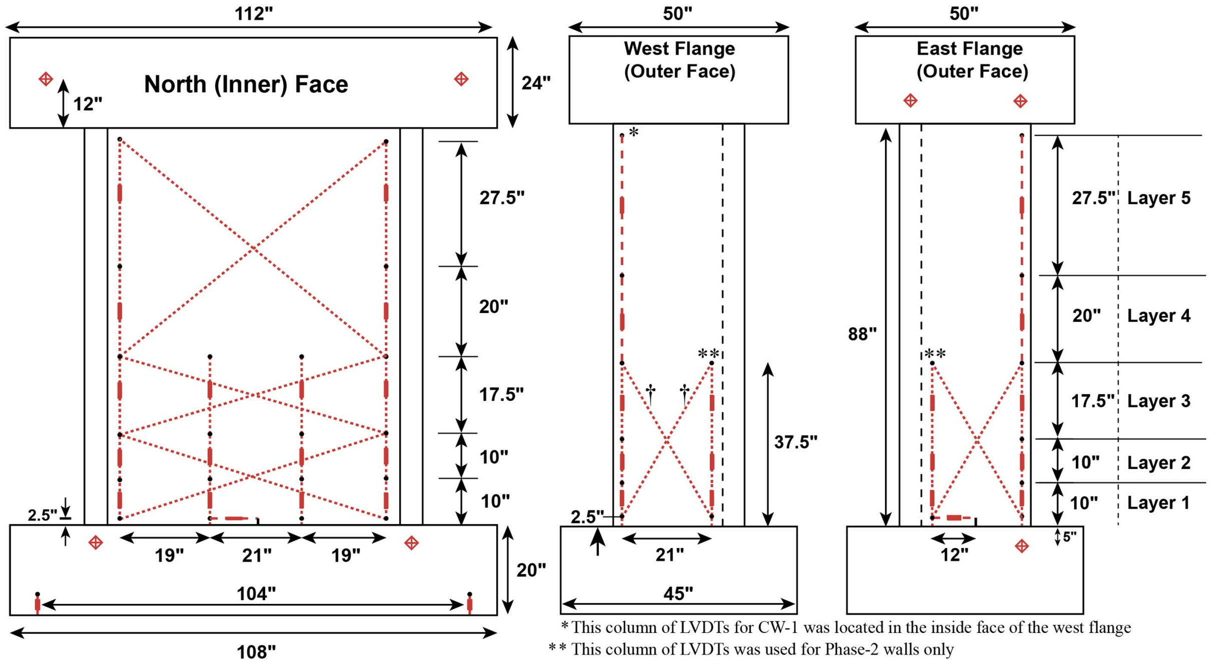

* This column of LVDTs for CW-1 was located in the inside face of the west flange
** This column of LVDTs was used for Phase-2 walls only
† These diagonal LVDTs were attached to the inside face of the west flange

Fig. 6. Instrumentation used to measure the local responses (not drawn to scale, units are in inches, 1 in. = 25.4 mm).

Axial load [$P_{\max} = 0.1A_g f'_c = 2{,}224$ kN (500 kips), where A_g is the gross sectional area of the walls] was applied using four 556-kN (125-kips) capacity hydraulic jacks located at the four corners of the top cap. The specimens were attached to the loading beam at the centroid of the top cap, which was also aligned with the center of mass of the walls. Applying the in-plane shear load through the center of the mass of the C-shaped specimens resulted in eccentric loading with the shear center of the specimens. The torsional moment demands resulting from this eccentricity were resisted by the two horizontal OOP actuators. Details associated with the applied loading protocols are discussed in the next section.

The test specimens were instrumented with more than 60 LVDTs (Figs. 6 and 7) to measure the wall flexural deformations, shear deformations, vertical slip deformations at the wall–footing

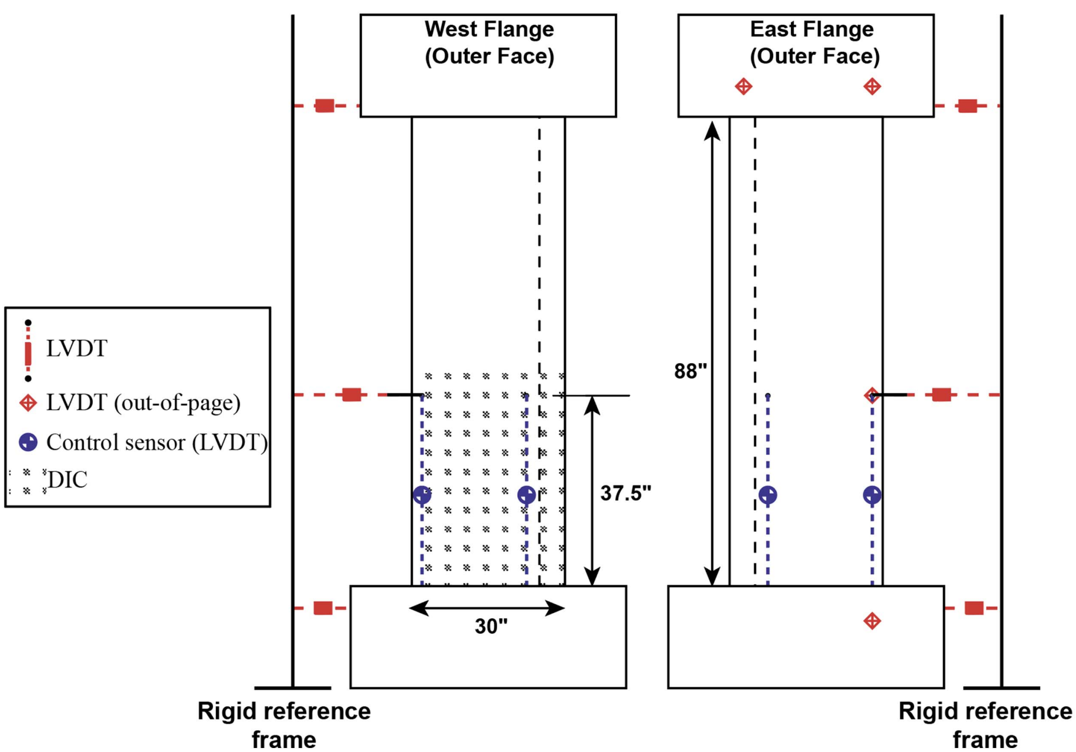

Fig. 7. Instrumentation used to measure the global responses (not drawn to scale, units are in inches, 1 in. = 25.4 mm).

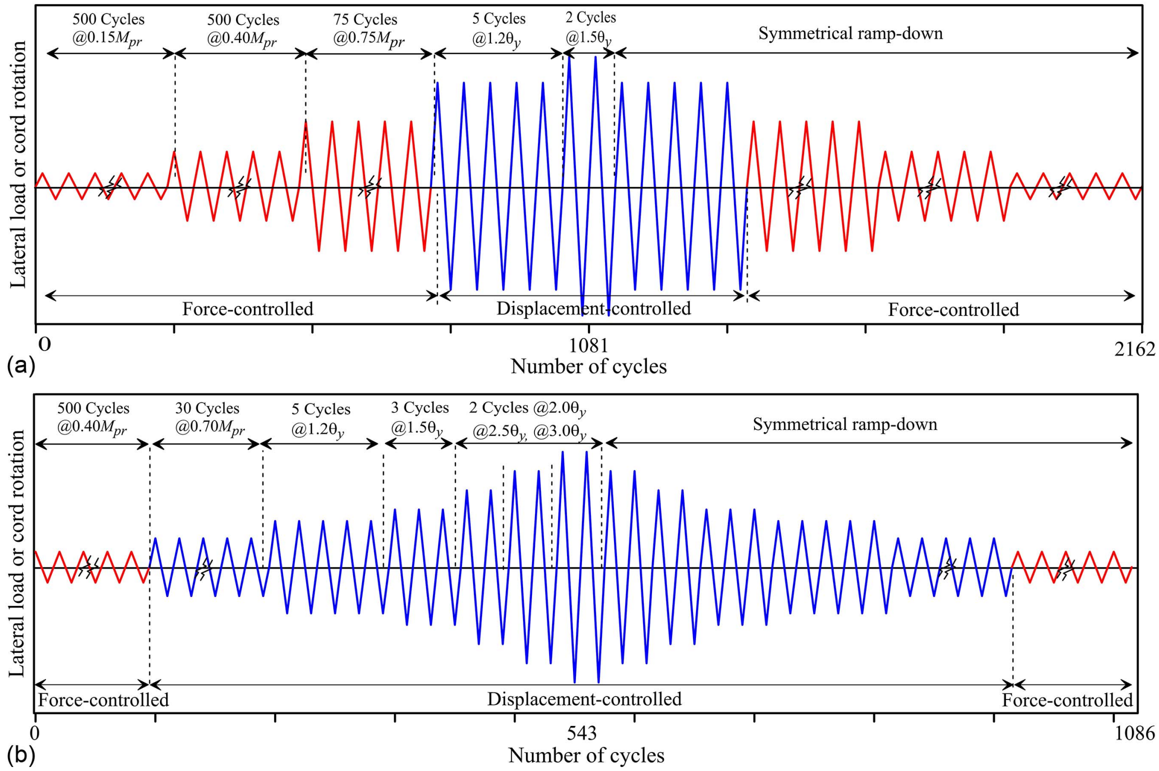

Fig. 8. (a) Coupling beam WLP; and (b) C-Wall WLP.

interface, shear sliding (horizontal) displacements at the wall–foundation interface, lateral displacements both in the in-plane and out-of-plane directions of the wall, top cap, and the footing, and any uplift of the footing from the laboratory strong floor. Also, four LVDTs (control sensors) (Fig. 7), attached to the wall footings on one end and to wall flanges at a height of 37.5 in. ($L_p = l_w/2$) on the other end, were used to calculate the plastic hinge rotation during the test to apply the prescribed WLP. A total of 32 strain gauges were used to measure the strains of the longitudinal and transverse reinforcement, U-bars, and crossties (Unal 2024). Finally, a digital image correlation (DIC) system was used to compute the surface displacements and strains of the web and west flange outer surfaces (Fig. 7).

Wind Loading Protocol

The WLP used for the testing of the C-walls was based on the protocol used by Abdullah et al. (2020, 2021) for coupling beam tests [Fig. 8(a)]. The coupling beam WLP was developed using the results of a nonlinear response history analysis of a 58-story building with a coupled core wall MWFRS subjected to loading histories recorded from wind tunnel tests. The WLP used for the wall tests is shown in Fig. 8(b), where M_{pr} was calculated in accordance with ACI 318-25 for 1.25f_y, and θ_y is the hinge yield rotation ("Instrumentation" section). The changes made to the coupling beam WLP are summarized as follows, and more detailed explanations have been given by Unal (2024):

- Force-controlled cycles at 0.15M_{pr} were omitted because, at a gravity axial loading of 0.1$A_g f'_c$, wall strain demands on the cross section would be in compression, and 75 cycles at 0.75M_{pr} were replaced with 30 displacement-controlled cycles at 0.7M_{pr}, which approximately represents first yield of wall flange longitudinal reinforcement, based on discussions with the PAC that 30 cycles was sufficient.
- The number of cycles at 1.5θ_y was increased to three to be consistent with common practice of applying three cycles for inelastic cycles.
- Inelastic rotation demands were increased to 3θ_y (from 1.5θ_y) to evaluate performance under higher-than-expected PBWD demands; however, two, versus three, cycles were applied because demands exceeding 1.5θ_y were considered higher than would be required at wall critical sections for PBWD.

The applied loading was unidirectional (parallel to the web, Positions A and D in Fig. 9), except for the inelastic cycles, where biaxial loading was applied (Positions B, C, E, and F), The force demands in the OOP direction were chosen as one-half of the OOP probable moment capacities (0.5$M_{pr,\mathrm{OOP}}$) based on discussions with the PAC. A constant axial load of $P = 0.1A_g f'_c = 2{,}224$ kN (500 kips) was used for the Phase I tests. For Phase II tests, the axial load was varied during OOP loading to simulate the variation of axial load on the C-shaped walls due to coupling beam shear forces. Based on input from PAC, the axial load was decreased to 0.05$A_g f'_c$ and 0.075$A_g f'_c$ for CW-3 and CW-4, respectively, during biaxial

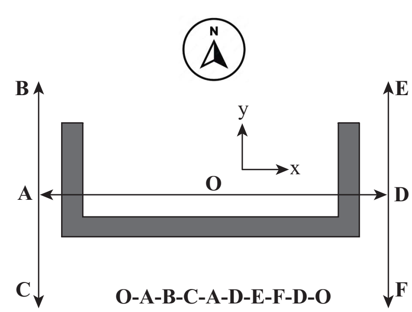

Fig. 9. Biaxial loading scheme.

(OOP^+) loading when flange edges were in compression (Positions B and E); however, due to test setup limitations, the axial load was limited to $0.1A_g f'_c$ for the negative OOP (OOP^-) loading with the web in compression (Positions C and F).

The maximum shear stress for IP loading ($\nu_{@M pr,\mathrm{IP}}$) during testing was limited to $2.60\sqrt{f'_c}$ for CW-1 and $4.25\sqrt{f'_c}$ for CW-2, CW-3, and CW-4, respectively, based on discussions with the PAC. The ratio of maximum base moment to base shear for in-plane loading ($M_{pr,\mathrm{IP}}/V_{@M pr,\mathrm{IP}}$) resulted in an effective height of 9.0 m (29.5 ft) for the roughly 1/3-scale test specimens, which approximately represents the effective height of a 12-story core wall with a story height of 3 m (9.8 ft).

Experimental Results

In the following subsections, experimental results are summarized, including observed damage, load–deformation responses, calculated lateral stiffness values for in-plane loading, measured axial strains, and observations related to the effect of lap splices on the wall behavior. This paper focuses on the experimental results under the applied WLP. Detailed results for the SLP and results of modeling studies have been provided by Unal (2024) and Unal and Wallace ("Nonlinear modeling of C-shaped reinforced concrete walls tested under wind and seismic loading protocols," submitted, *J. Struct. Eng.*, ASCE, Reston, Virginia).

Observed Damage

Specimen CW-1, with $\rho_l = 0.75\%$, showed no damage (e.g., concrete spalling, concrete crushing, longitudinal bar buckling, or bar fracture) after the completion of the WLP. DIC analysis results showed minor, uniformly distributed horizontal flexural cracks within the flanges and diagonal tension (shear) cracks within the web above the splice region, with the biggest cracks located right above the splice and at the wall–footing interface. After completion of the WLP, residual flexural crack widths within the flanges were measured to be 0.1 mm, and residual diagonal web cracks were negligible in width.

Unlike CW-1, a significant amount of damage, due to the higher reinforcement ratio resulting in higher compressive strain demands, was observed for CW-2 (with $\rho_l = 1.5\%$). After the completion of ramp-up cycles (cycles up to and including the $3.0\theta_y$ demands), concrete spalling was observed at the base of the west flange and the flange–web corners. Although the ramp-down cycles did not result in more damage at the west flange or the flange–web corners, concrete spalling, core concrete crushing (23% of the total length of the flange was crushed), and longitudinal bar buckling were observed at the base of the east flange edge after the WLP was completed. Figs. 10 and 11 show the progression of the damage observed at the east flange during the WLP and the damage state of the west flange after the WLP.

For the Phase II walls (CW-3 and CW-4), the damage observed at the flange–web corners was almost identical with that of CW-2, i.e., cover spalling up to approximately 0.5 m (20 in.), (equal to the splice length) above the footing. However, due to the improved detailing provided at the flange edges and the reduction in axial stress during the OOP^+ loading, the flange edges were less damaged for CW-3 and CW-4 compared with CW-2. Only minor concrete crushing was observed at the base of the east flange edge for CW-3, whereas for CW-4, buckling and fracture of only the outer layer vertical reinforcement at the base of the flange was observed (Fig. 12). Similar to CW-1, the largest crack openings were observed right above the splice region and at the wall–footing interface, and only hairline cracks were observed within the splice region.

Load–Deformation Responses

Base Moment–Hinge Rotation

The IP base moment–plastic hinge rotation responses determined using the control sensors (Fig. 7) for all specimens are shown in Figs. 13(a and b), where the rotation demands were calculated using estimated hinge yield rotations (θ_y) values of 0.1% for CW-1 and 0.3% for CW-2, CW-3, and CW-4, respectively. Detailed data analysis (Unal 2024) after testing CW-2 showed that the hinge yield rotation was closer to 0.25% ($\theta_{y,\mathrm{exp}}$); therefore, the maximum hinge rotation ductility (μ_θ) applied was approximately $3.6\theta_y$ as opposed to $3.0\theta_y$ as prescribed by the WLP [Fig. 8(b)]. No IP strength loss was observed for any of the specimens, and given that CW-2, CW-3, and CW-4 had the same longitudinal reinforcement ratios and axial load applied during in-plane loading, the responses are very similar [Fig. 13(b)].

(a) (b) (c)

Fig. 10. East flange edge of CW-2: (a) after the ramp-up cycles; (b) after the inelastic ramp-down cycles; and (c) after the completion of WLP.

J. Struct. Eng., 2026, 152(1): 04025228

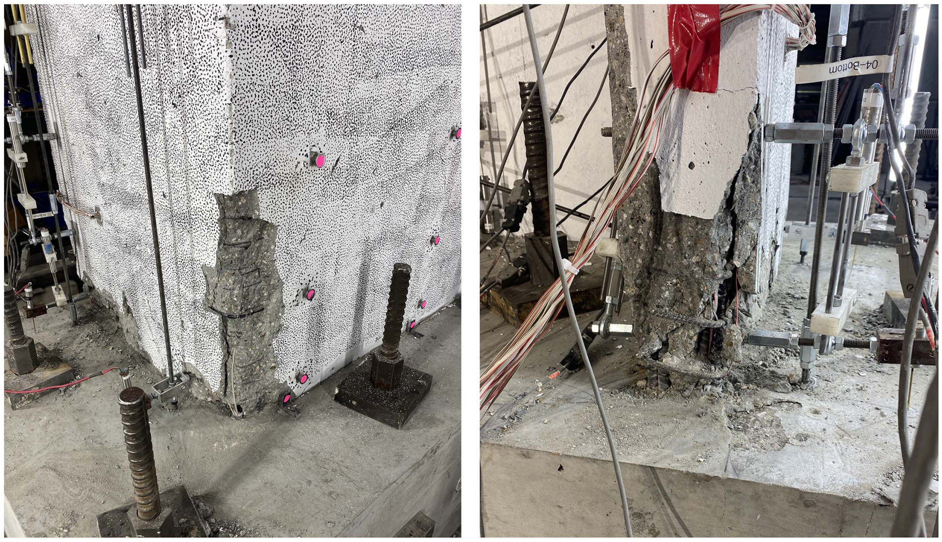

(a) (b)

Fig. 11. CW-2: (a) west flange–web corner; and (b) west flange edge after the completion of WLP.

Analytical predictions (Fig. 13) were determined by integrating moment versus curvature results computed for expected material properties (Tables 1 and 2) over the assumed hinge length of $l_w/2$ above the wall–foundation interface. The effects of the lap splice and slip/extension deformations on the predicted curvature distribution were not considered. The predicted hinge rotations matched the experimental results, i.e., flexural stiffness (uncracked and cracked), yield moment, and postyield responses, very closely. These results indicate that modeling approaches commonly used for PBWD of tall buildings (uniaxial material models for expected material properties, plane-sections remain plane, no special modeling of the splice region, and neglecting slip/extension) reasonably capture the IP moment–rotation responses. However, for walls without lap splices, neglecting the slip/extension deformations might overestimate flexural stiffness because the added flexibility of the slip/extension deformations appears to be offset by the lower curvatures that occur over the splice region for these tests ("In-Plane Lateral Stiffness for Linear Analysis" section and Table 5).

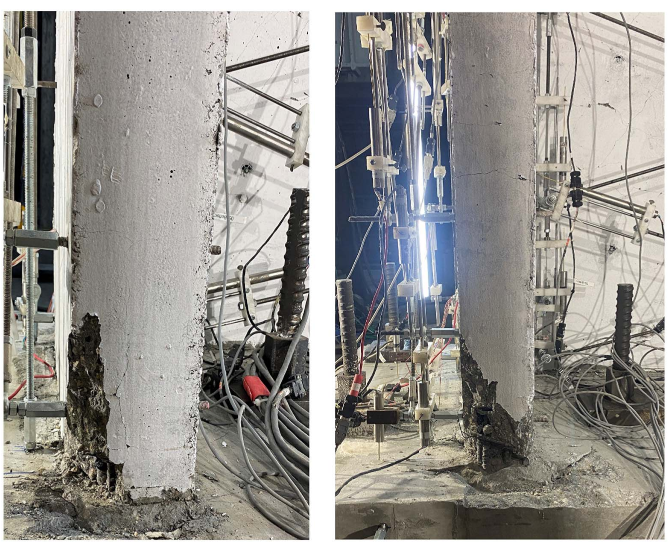

(a) (b)

Fig. 12. East flange of (a) CW-3; and (b) CW-4 after the completion of WLP.

The OOP base moment–plastic hinge rotation responses are given in Figs. 14(a and b) for the ramp-up and ramp-down cycles, respectively, for $\rho_l = 1.5\%$ specimens only, because no stiffness degradation (other than concrete cracking) or strength loss was observed for CW-1. Due to concrete crushing at the base of the flange edges, stiffness degradation was observed for CW-2 and CW-4 during the ramp-up cycles in the OOP $+y$ direction (Positions B and E). No OOP strength loss was observed for CW-4 during the ramp-down cycles; however, the OOP$^+$ base moments decreased from 675 k-ft (915.2 kN-m) to 230 k-ft (311.8 kN-m), a 66% strength loss, for CW-2 at the end of the WLP. Neither OOP strength loss nor stiffness degradation was observed for CW-3.

The approach used to determine the required detailing at the flange edges for the Phase II walls ("Specimen Design" section) was successful in preventing strength loss in the OOP$^+$ direction that was observed for CW-2; however, stiffness degradation was observed for CW-4 (in the OOP$^+$ direction). Eliminating or reducing stiffness degradation could likely be accomplished by reducing the spacing of the hoops and crossties provided at the flange edges; however, additional tests or relatively complex nonlinear models would be required to investigate this issue; this topic is beyond the scope of this paper.

Base Shear–Top Lateral Displacement

The in-plane base shear–drift ratio responses, calculated using the average displacements recorded by the two horizontal LVDTs attached to the east side of the top caps (Fig. 6), are shown in Figs. 15(a and b) for $\rho_l = 0.75\%$ and $\rho_l = 1.5\%$ specimens, respectively, where the displacement ductility values (μ_Δ) were calculated using effective yield drift ratio values of 0.15% and 0.4%, respectively. The lateral displacements measured at the top of the walls due to sliding and rotation of the footing were removed. Because in-plane plastic hinge rotation demands were controlled during testing, versus lateral drift ratios, and because of the different amounts of damage that occurred over the hinge region for the $\rho_l = 1.5\%$ specimens, different drift ratios were observed for different walls [Fig. 15(b)].

At the maximum hinge rotation demands of the WLP (0.9% for the $\rho_l = 1.5\%$ specimens), the in-plane drift ratios were higher, ranging from 1.5% to 2.1%. The drift values were significantly higher

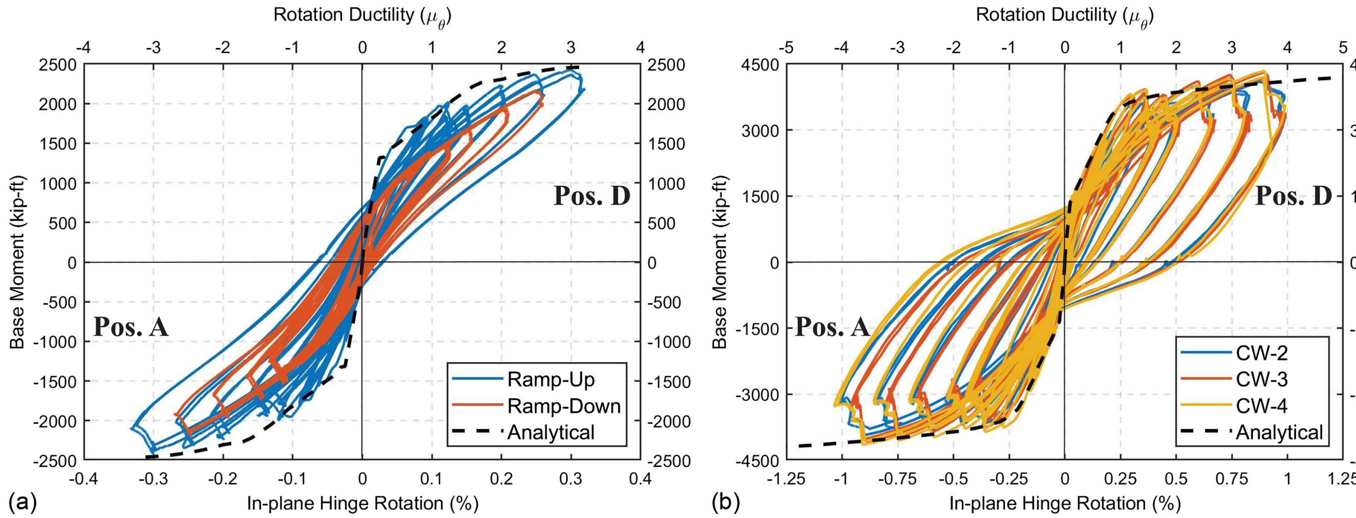

Fig. 13. In-plane base moment–hinge rotation responses of (a) CW-1 during ramp-up and ramp-down cycles; and (b) CW-2, CW-3, and CW-4 during ramp-up cycles only (1 kip-ft = 1.36 kN-m).

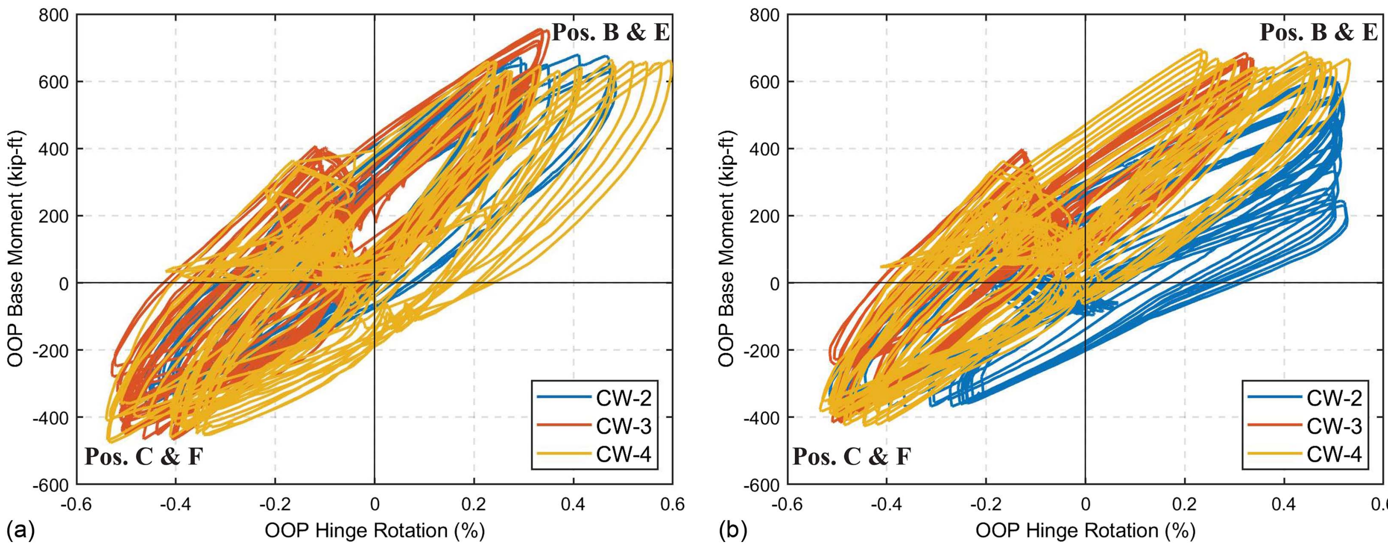

Fig. 14. Out-of-plane base moment–hinge rotation responses of CW-2, CW-3, and CW-4: (a) during ramp-up; and (b) ramp-down cycles (1 kip-ft = 1.36 kN-m).

than the hinge rotation values because of (1) the low curvature/rotation demands occurred over the splice regions [$l_s = 0.5$ m (20 in.)], which accounted for 53.3% of the plastic hinge length [$L_p = 0.95$ m (37.5 in.)] but only 22.7% of the total wall height [2.23 m (88 in.)], and (2) the inelastic curvatures that occurred above the hinge region. The results suggest that overlapping longitudinal reinforcement stiffens and strengthens the splice region such that inelastic curvatures spread over a greater height (above the splice). This issue is addressed in more detail in the discussion related to moment-curvature responses. A decrease was observed in the in-plane base shear demands for all the walls during biaxial loading application because the in-plane deformations were kept constant during the out-of-plane loading application, not the applied forces.

The total in-plane lateral displacement (δ_{tot}) of the walls can be expressed as the sum of the flexural and shear deformations over the wall height [Eq. (3)]. Flexural deformations include the curvature/rotation of the wall ($\delta_{f,\mathrm{wall}}$) and the deformations due to the slip/extension at the wall–footing interface (δ_{slip}). Shear deformations include the pure translation (shear distortion) along the height of the wall ($\delta_{s,\mathrm{wall}}$), and the shear sliding along the wall–footing interface ($\delta_{s,\mathrm{slide,wall}}$)

$$\delta_{\mathrm{tot}} = \delta_{f,\mathrm{wall}} + \delta_{f,\mathrm{slip}} + \delta_{s,\mathrm{wall}} + \delta_{s,\mathrm{slide,wall}} \tag{3}$$

The flexural, slip/extension, and shear sliding deformations were calculated using LVDTs attached to the walls. The wall shear deformations ($\delta_{s,\mathrm{wall}}$) were calculated using two different approaches. For the first approach (A1), any deformation not associated with flexure, slip/extension, or shear sliding was attributed to shear distortion. For the second approach (A2), the diagonal LVDTs attached to the inner surface of the web (Fig. 6) were used. More details regarding the two approaches have been given by Unal (2024). Fig. 16 shows the base shear–drift ratio responses of each

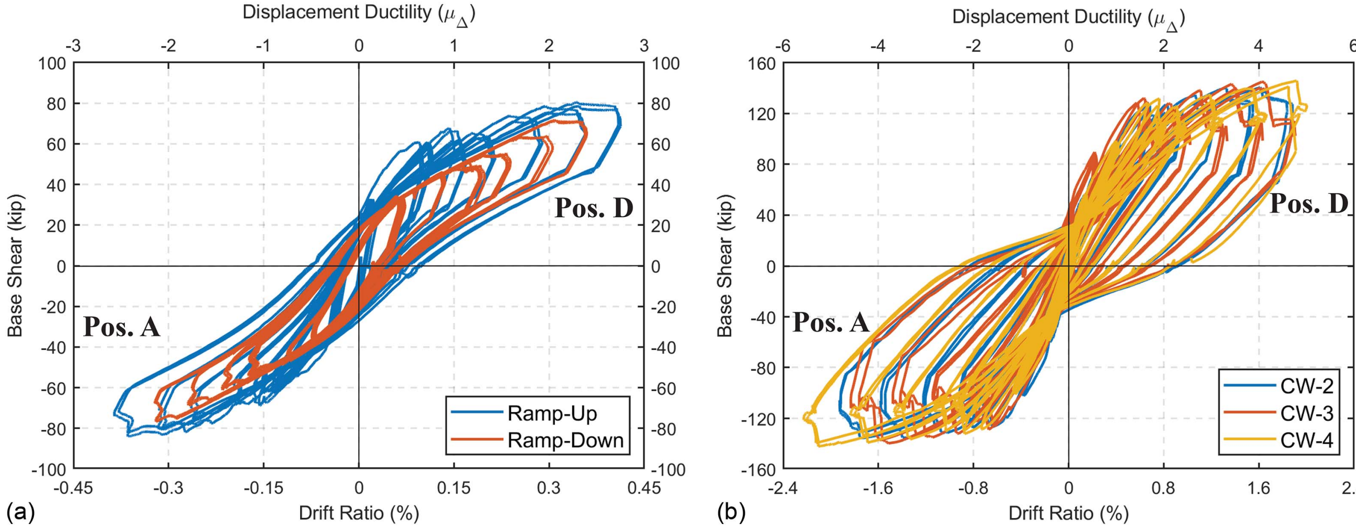

Fig. 15. In-plane base shear–drift ratio rotation responses of (a) CW-1 during ramp-up and ramp-down cycles and (b) CW-2, CW-3, and CW-4 during ramp-up cycles only (1 kip = 4.45 kN).

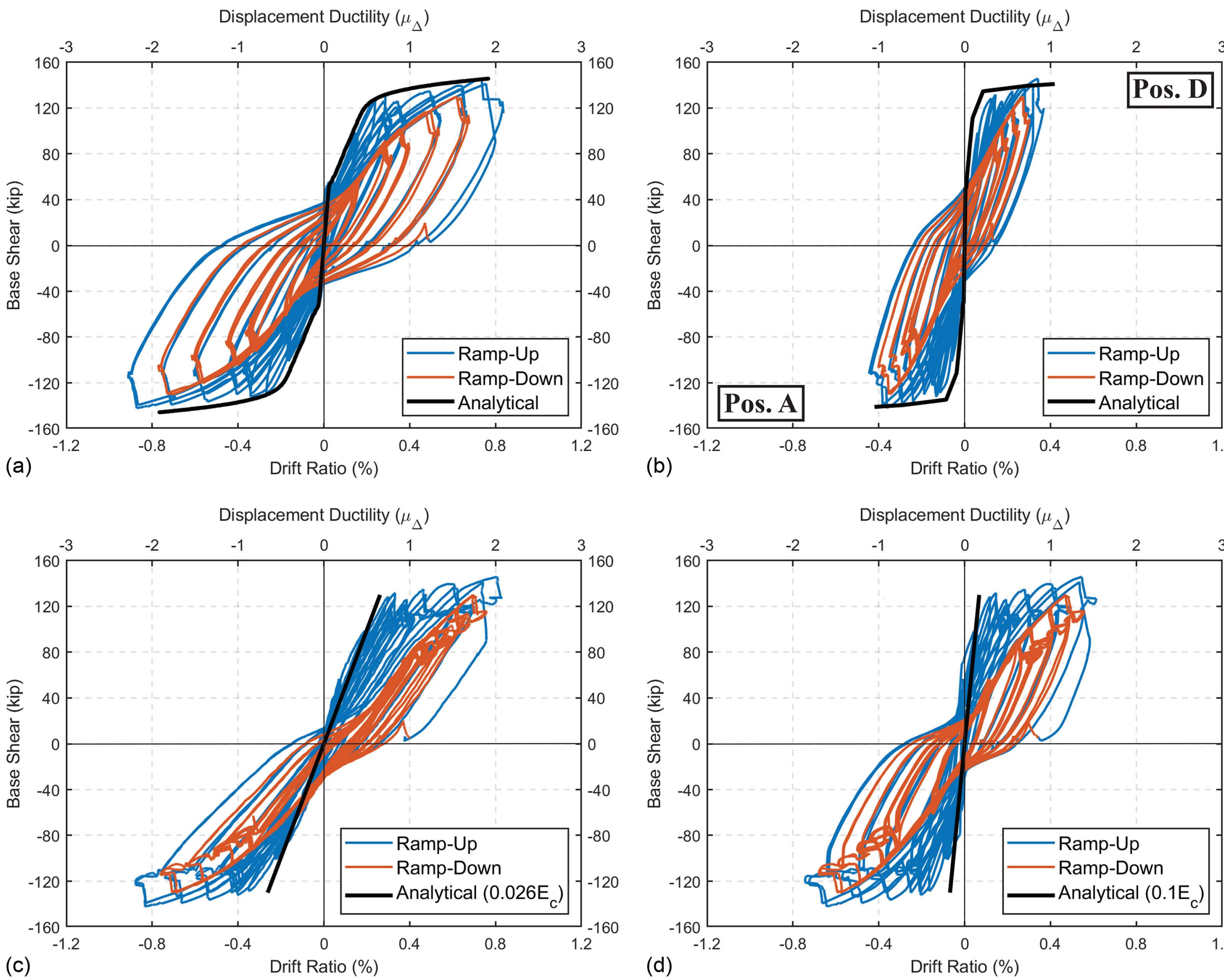

Fig. 16. Different components of in-plane base shear-drift ratio response of CW-4: (a) flexural; (b) slip/extension; (c) shear (A1); and (d) shear (A2) deformations (1 kip = 4.45 kN).

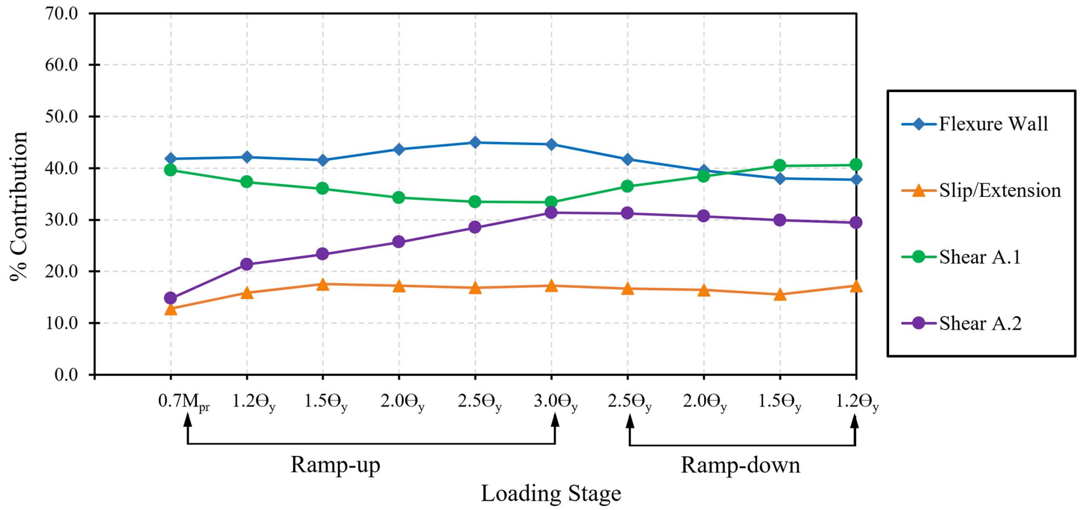

Fig. 17. Average contributions of flexure, slip/extension, and shear deformations to the total lateral displacement at the top of the walls.

displacement component for CW-4 during the ramp-up and ramp-down portions of the WLP, which are representative of all tests [Unal (2024) has given the results of the other tests].

The relative contributions of each displacement component to the total displacement at the top of the walls were also calculated at various hinge rotation levels for both positive and negative in-plane loading. The average contributions determined for positive and negative loading for CW-2, CW-3, and CW-4 are shown in Fig. 17. In general, at the maximum hinge rotation demands ($3.0\theta_y$), the flexural ($\delta_{f,\text{wall}}$), shear ($\delta_{s,\text{wall}}$), and slip/extension (δ_{slip}) deformations contributed approximately 45%, 30%, and 20%, respectively, to the total lateral displacement at the top of the walls. Similar values were observed for CW-1, i.e., 50%, 25%, and 20%, respectively.

The test walls represented approximately the bottom two stories of a 12-story core wall. For a 12-story wall, the flexural drift ratios due to plastic hinge rotations are essentially constant along the height of the wall (rigid body rotation), whereas shear deformations (pure translation) tend to decrease up the height of the wall. Therefore, the contribution of the shear deformations to the drift ratios at the top of a 12-story wall is expected to be smaller than the values calculated for the test specimens (e.g., Abdullah and Wallace 2019; Segura and Wallace 2018; Thomsen and Wallace 2004).

Moment-curvature analysis results calculated using expected material properties were also used to predict the monotonic base shear–top displacement response due to flexural deformations [Fig. 16(a)] using Eq. (4)

$$\delta_{f,\text{wall}} = \sum_{i=1}^{n} \theta_i (h_{\text{wall}} - x_i) \approx \sum_{i=1}^{n} (\bar{\phi}_i h_i)(h_{\text{wall}} - x_i) \tag{4}$$

where θ_i = rotation of layer i (estimated as the area under the curvature distribution $\bar{\phi}_i h_i$, where $\bar{\phi}_i$ is the average curvature over layer i and h_i is the height of layer i); x_i = distance to the centroid of the average curvature distribution of layer i; and h_{wall} = height of the wall.

For the predictions, five layers ($n = 5$) were used (to match the layers of LVDTs used during testing), and h_i values were taken from the LVDT layers (Fig. 6) used during testing. Over the splice region, Layer 1 (for CW-1) and Layers 1 and 2 (for CW-2, CW-3, and CW-4), the curvature values from the moment-curvature analysis were divided by 4.0 to account for the significantly lower curvature values (higher stiffness) that were observed over the splice regions in the test walls ["Moment-Curvature" section and discussed by Unal (2024)]. Like the moment–rotation predictions, the results indicate good matches [Fig. 16(a)] for stiffness prior to, and after concrete cracking, and good comparisons for $V_{@My}$ and $V_{@Mpr}$ (e.g., predicted to tested ratios of 1.06 and 1.02, respectively, for CW-4).

The displacements at the top of the walls due to slip and extension deformations (δ_{slip}) were estimated as follows:

$$\delta_{\text{slip}} = \theta_{\text{slip}} h_{\text{wall}} = \Delta_{\text{slip}}(d - c) h_{\text{wall}} \tag{5}$$

where θ_{slip} = rotations due to slip/extension deformations (Δ_{slip}); d = effective depth; and c = neutral axis depth, which was calculated using the analytical moment-curvature predictions. The model proposed by Alsiwat and Saatcioglu (1992) was used to predict Δ_{slip}, which is compared with the experimental results in Fig. 16(b). In general, the analytical model resulted in lower values than the experimental values before yielding; however, the model matched the experimental slip/extension deformations more closely at $V_{@Mpr}$ [Fig. 16(b)].

For wall shear deformations, various shear stiffness values have been recommended, e.g., $0.4E_c$ (commonly used for linear wind design), $0.2E_c$ (LATBSDC 2023), $0.13E_c$ [FEMA P-2208 (FEMA 2023)], $0.02E_c$ [PEER/ATC 72 (PEER and ATC 2010)], and $0.01E_c$ (Kolozvari et al. 2021). Secant-to-first yield shear stiffness values of $0.026E_c$ [Fig. 16(c)] and $0.10E_c$ [Fig. 16(d)] matched the experimental results reasonably well, depending on the approach used to determine shear deformations. The value of $0.10E_c$ determined with the web LVDTs [Fig. 16(d)] appears less reliable due to the low values of LVDT readings; the value of $0.026E_c$ is closer to results for slender walls reported previously by PEER/ATC 72 and Kolozvari et al. (2021). Therefore, the use of shear stiffness values of $0.02E_c$ to $0.10E_c$ appears reasonable; for building analysis and design, sensitivity studies (e.g., for a single input record) should be conducted to assess the sensitivity of responses to the value of shear stiffness used.

After completion of the WLP, either uniaxial or biaxial SLPs were applied to each test wall. The maximum lateral drift ratios reached during either the WLP or the SLP prior to significant lateral strength loss were 2.8%, 1.6%, 3.3%, and 2.4% for CW-1, CW-2,

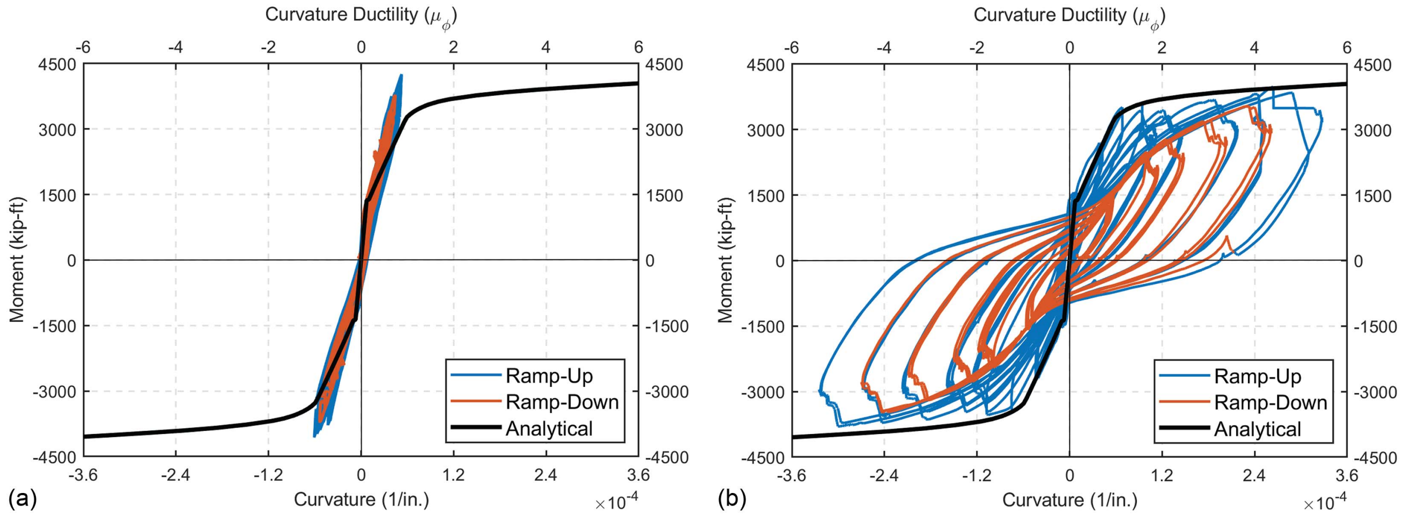

Fig. 18. Moment-curvature response of CW-4: (a) at the splice region (Layer 1); and (b) above the splice region (Layer 3) (1 kip-ft = 1.36 kN-m).

CW-3, and CW-4, respectively. Damage at significant strength loss consisted of concrete crushing and bar buckling above the splice region at the west flange for CW-1, concrete crushing and bar buckling at the base of the east flange for CW-2, OOP instability of the east flange for CW-3, and concrete crushing and bar buckling at the base of the east flange during the biaxial seismic loading for CW-4. More details on the SLPs used, the observed damage, and measured responses during the SLPs have been given by Unal (2024).

Moment-Curvature

The in-plane moment-curvature responses over the height of the wall were estimated using columns of LVDTs attached at the edges of the flanges, along the web (four columns), and at the corners of the flanges (for Phase II walls only) (Fig. 6). The LVDTs at Layer 1 spanned between 2 and 10 in. above the footing (2–10 in.), whereas Layers 2, 3, 4, and 5 were over heights 10–20, 20–37.5, 37.5–57.5, and 57–85 in., respectively (Fig. 6). In accordance with the lack of damage observed within the splice region, i.e., hairline cracks only, the curvature values calculated using the LVDTs within the splice region (Layer 1 for CW-1, and Layers 1 and 2 for CW-2, CW-3, and CW-4) were significantly smaller than the calculated curvature values above the splice region. The largest curvature values were observed for the layers right above the splice regions for all the specimens, where the largest crack widths were observed.

Fig. 18 shows the moment-curvature responses of CW-4 during the ramp-up and ramp-down portions of the WLP for Layers 1 and 3, where the moment values were calculated at the midheight of the LVDT layers. The responses for all the specimens calculated using different layers of LVDTs has been given by Unal (2024). In general, the analytical moment–curvature relations calculated (1) using the tested material properties, (2) assuming the plane section remain plane, and (3) neglecting the lap splices and slip/extension deformations closely match the experimental responses [Fig. 18(b)] (Unal 2024) in terms of stiffness (for the regions above the splice region) and strength. As mentioned previously ("Base Moment–Hinge Rotation" section), this observation suggests that the plane sections remain plane assumption produces reasonable results and can be used for core walls, as noted previously by others (e.g., Kolozvari et al. 2021). Although more sophisticated modeling approaches are available (Kolozvari et al. 2022; Tura et al. 2024), currently, they are not practical for tall building design.

The maximum base moment observed during testing ($M_{\max}$) occurred at $3.0\theta_y$ and was compared with the nominal (M_n) and probable (M_{pr}) moment capacities of the walls calculated based on the ACI 318-25 provisions. For walls CW-2, CW-3, and CW-4 ($\rho_l = 1.5\%$), the average value of $M_{\max}$ for the three specimens was $M_{\max} = 1.01M_{pr}$, whereas for CW-1 ($\rho_l = 0.75\%$), $M_{\max}$ was equal to $1.03M_n$ and $0.94M_{pr}$. Therefore, for the calculation of wall flexural strength under limited nonlinear wind demands, ACI 318-25 approaches can be used to calculate M_n and M_{pr}.

Base Moment–Hinge Rotations (Impact of Lap Splices)

As mentioned previously, only hairline flexural cracks were observed within the splice regions of the walls. The observed damage was consistent with the curvature calculations, i.e., significantly lower curvature values were calculated over the splice region compared with the regions above the splices (Fig. 18). Therefore, the lap-spliced longitudinal reinforcement stiffened and strengthened the splice region, resulting in a shifting of the nonlinear deformations to the region above the splice. To study this issue, two more approaches were used to compute hinge moment–rotation relations for assumed plastic hinge regions of (1) $l_w/2$ located above the splice, i.e., rotations were calculated using Layer 3 (spanning 20–37.5 in.), Layer 4 (37.5–57.5 in.) LVDTs, and the LVDTs at the wall–footing interface (to include the slip/extension deformations); and (2) $l_w/2 + L_s$, calculated using the control sensors (over $l_w/2$), which include slip/extension at the wall–foundation interface, and Layer 4 LVDTs (37.5–57.5 in.).

Results for IP base moment–hinge rotation responses are presented in Fig. 19 for CW-4 and indicated that the results are similar because the flexural deformations over the splice length are small relative to the region above the splice and at the wall–foundation interface. Due to the simplicity of the second approach, it was used for the other specimens (Fig. 20) and resulted in roughly a 10% increase at the maximum rotation for CW-1 (from 0.3% to 0.33%) [Fig. 20(a)], and up to a 53% increase for the $\rho_l = 1.5\%$ specimens (from −0.9% to −1.38% for CW-4) [Fig. 20(b)].

Axial Strains

Axial strains were measured using columns of LVDTs attached at the flange edges, the web inside surface, and the flange–web corners (only for Phase II walls) (Fig. 6). The largest tensile strains were measured above the splice in Layer 2 for CW-1 and Layer 3 for the other walls, whereas the largest compressive strains were measured at the base of the walls (at Layer 1). Fig. 21 shows the

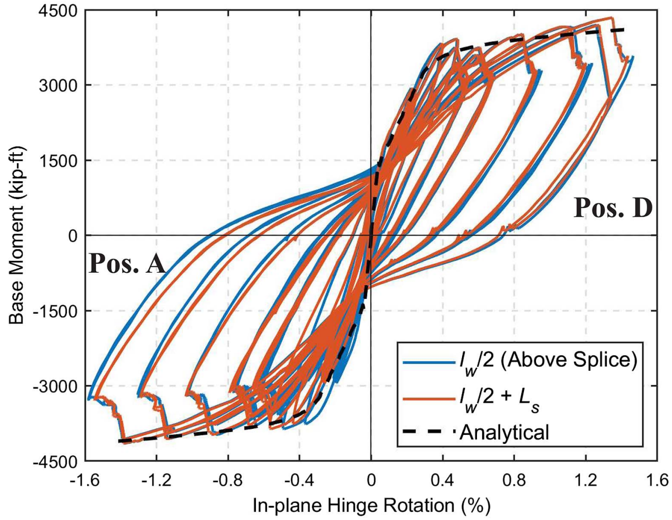

Fig. 19. Comparison of the in-plane base moment–hinge rotation responses of the two different approaches used (1 kip-ft = 1.36 kN-m).

tensile and compressive strains measured for CW-4 using the LVDTs at the west flange edge along the height of the wall at different loading positions and different load steps of the WLP. Results for other walls and load steps have been presented by Unal (2024).

The maximum compressive strains at $3.0\theta_y$ were greater than the compressive strain at peak stress (Fig. 21) of the cylinder tests (~0.003) (Table 1), suggesting some concrete compression softening; however, because the LVDTs were located several centimeters from the face of the concrete surface (Fig. 11) and neutral axis depths are relatively small, the surface concrete compressive strains might be significantly smaller than recorded at the LVDT. To assess this issue, tension and compression strain demands on the wall concrete surfaces at $3\theta_y$ in-plane hinge rotation demands, before the application of OOP moment demands, were estimated using the LVDT recordings, the LVDT distances from the concrete surfaces, and the neutral axis depths determined using LVDT readings.

For the $\rho_l = 1.5\%$ walls, the calculated peak surface tensile strains for the three walls were similar for IP loading (Table 3). However, significantly different peak surface compressive strains were calculated for CW-2 and the Phase II specimens (Table 3), with the largest values for the heavily damaged wall (CW-2) and lower values for walls with minimal concrete crushing observed at the base of the flange edges (CW-3 and CW-4). For the Phase II walls, strain demands gradually decreased during the ramp-down loading (Unal 2024); however, for CW-2, the peak compressive strain value increased to as high as −0.01 for the east flange during the ramp-down cycles (Table 3). The high compressive strain values calculated for ramp-down loading of CW-2 were consistent with the significant amount of damage (concrete core crushing and longitudinal bar buckling) that occurred during the ramp-down loading at the east flange edge, which was mainly due to the high level of axial load applied during OOP^+ loading and the detailing provided at the flange edges.

For Phase II walls, the surface strains at the flange–web corners were also calculated and compared with the values calculated at the flange edges. In general, during IP loading (Positions A and D), higher compressive strain demands were calculated at the base of the flange–web corners compared with flange edges (Table 3 and Fig. 22). In contrast, the tensile strain demands were similar.

The effect of biaxial loading on the tensile and compressive strains was also studied. Although the application of OOP bending increased the tensile strains by only a factor of 1.1 on average for the $\rho_l = 1.5\%$ specimens (Unal 2024), it had a more significant impact on the compressive strains (Fig. 22). In general, during OOP loading, compressive strains using LVDT readings at the base of the flange edges increased by a factor of approximately 2.0 during the lower IP hinge rotation cycles ($1.2\theta_y$ and $1.5\theta_y$) and by approximately a factor of 1.5 on average during the higher IP rotation cycles ($2.5\theta_y$ and $3.0\theta_y$). The application of OOP bending moments did not significantly affect the strain demands at the flange–web corner LVDTs (Fig. 22), possibly due to the location of the LVDTs, i.e., attached to the flange surfaces approximately 153 mm (6 in.) away from the corners (towards the flange edges) (Fig. 6). Similar comparisons for all the specimens at different layers of LVDTs were made by Unal (2024).

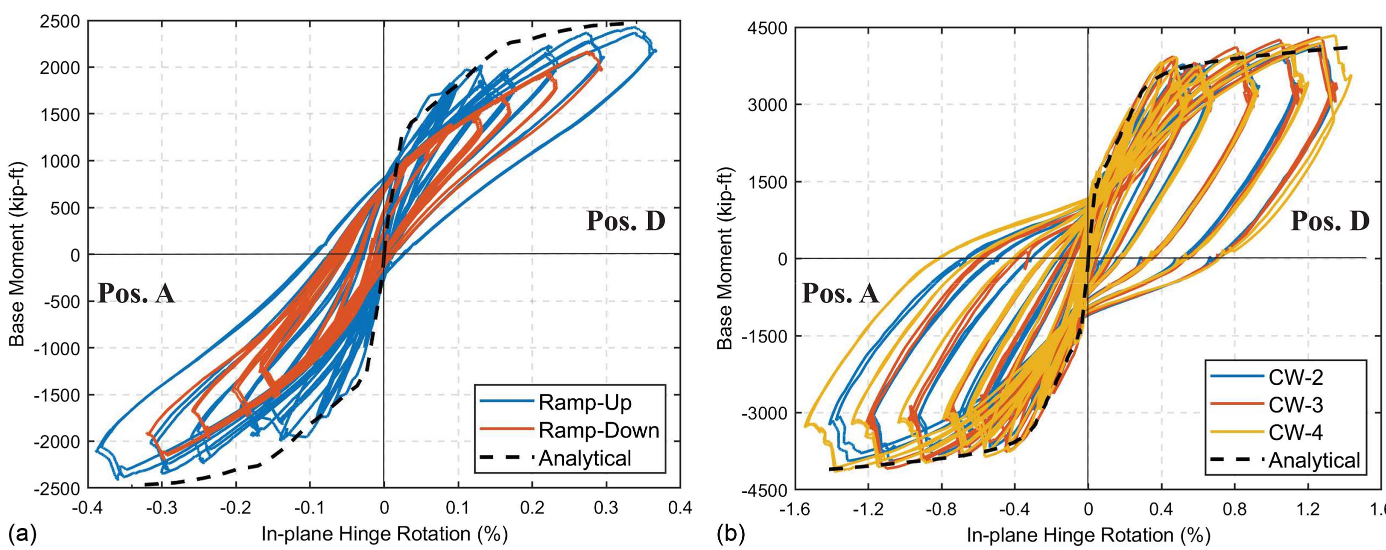

Fig. 20. In-plane base moment–hinge rotation responses (calculated using $L_p = l_w/2 + L_s$) of (a) CW-1 during ramp-up and ramp-down cycles; and (b) CW-2, CW-3, and CW-4 during ramp-up cycles only (1 kip-ft = 1.36 kN-m).

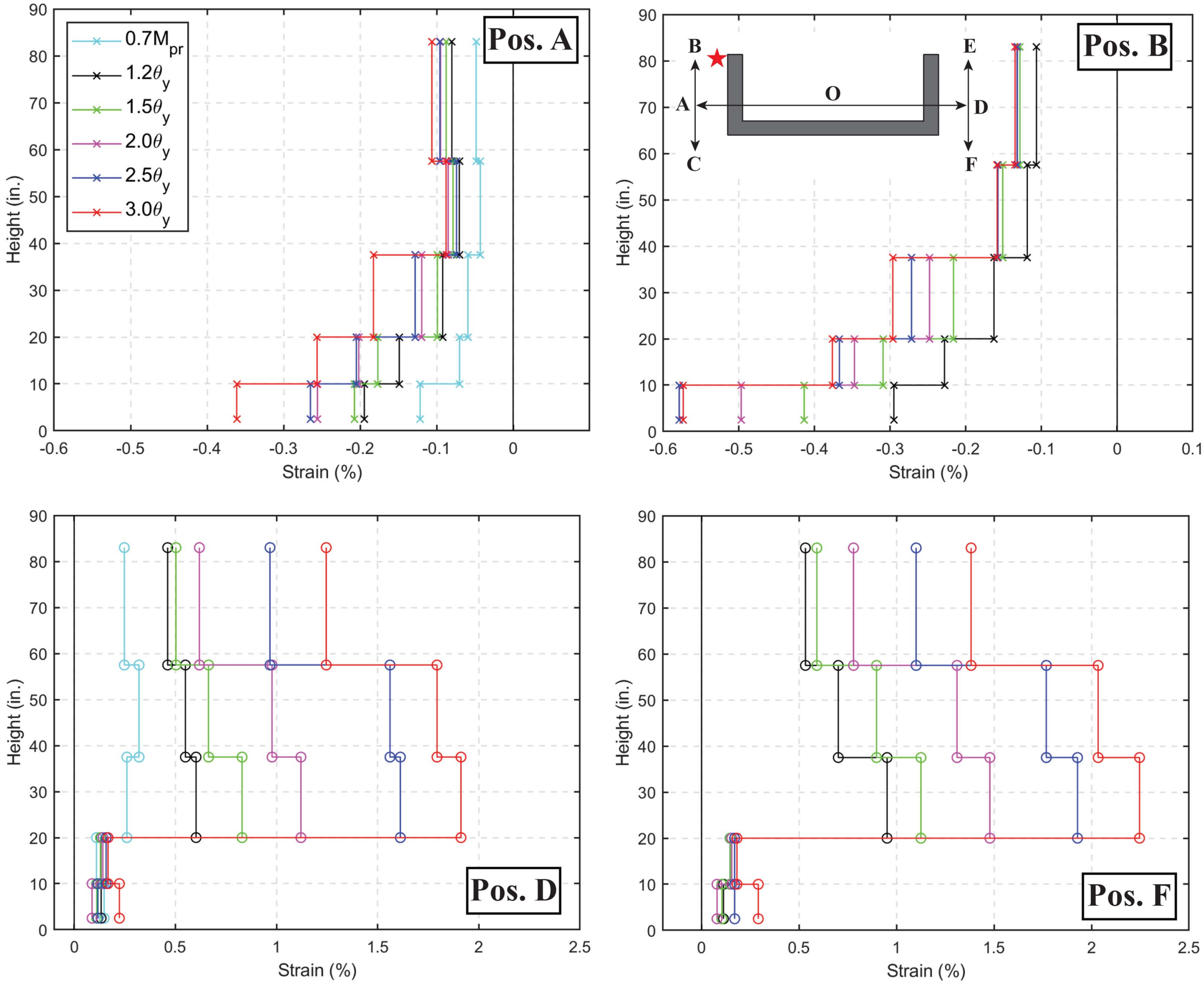

Fig. 21. Axial LVDT strain profiles of CW-4 along the height of the edge of the west flange (star) at different loading positions during the ramp-up loading of WLP (1 in. = 25.4 mm).

Strain-Based Acceptance Criteria for PBWD

The initiation of cover spalling and minor concrete core crushing was observed at concrete compressive strains (ε_c) of 0.0035–0.004, which were reached at $2.0\theta_y$ in-plane rotation demands (during the biaxial loading) for CW-2 and at $3.0\theta_y$ in-plane rotation demands (under biaxial loading, peak demand of the WLP) for the Phase II walls (due to the reduced axial stresses).

The lateral strength loss was observed for CW-2 when the concrete compressive strains at the base of the flange edges reached values of approximately 0.005–0.006, which was observed during the biaxial loading at $3.0\theta_y$ in-plane rotation demands. For the Phase II walls, because the maximum concrete surface compressive strains reached only 0.0045, no strength loss was observed.

Based on the results of this study, different peak compressive concrete strains are recommended for different ASCE prestandard performance objectives. For the operational performance objective, the strain limit was selected to prevent damage (except concrete cracking), i.e., cover spalling, concrete crushing, and bar buckling. Therefore, a value of $\varepsilon_c = 0.00375/1.5 = 0.0025$ is recommended. The average experimental value (0.00375) is divided by 1.5 to account for the uncertainties in computing the compressive strains using non-linear models (Kolozvari et al. 2021; Orakcal and Wallace 2006).

Based on the experimental results for the $\rho_l = 1.5\%$ specimens, flange edge compressive strains reach 0.0025 at around $1.0\theta_y$ in-plane rotation demands with OOP demands (biaxial loading). A value of 0.0025 is similar to the strain values at the peak concrete compressive strength calculated using unconfined concrete constitutive models (Kent and Park 1971; Chang and Mander 1997), i.e., prior to strain softening, suggesting that the strain at peak unconfined stress could also be used for this performance objective. On the other hand, for the continuous occupancy performance objective, a higher value, $\varepsilon_c = 0.0055/1.5 \approx 0.0037$, is recommended to prevent strength loss.

In addition to the peak compressive strain limits recommended previously, lower compressive strain limits are recommended in Table 4, depending on the number of cycles at or below the given strain limits. The values given in Table 4 are based on concrete surface strains estimated for CW-4 (under biaxial loading) because the

Table 3. Calculated peak surface tensile and compressive strain demands

Specimen	LVDT location	Tensile strain	Compressive strain
CW-1	Flange edge	0.005	−0.0008
CW-2	Flange edge	0.018	−0.0044 −0.01[a] (RD)
CW-3	Flange edge Flange–web corner	0.016 —[b]	−0.0029 −0.0034
CW-4	Flange edge Flange–web corner	0.021 0.018	−0.0027 −0.0040

Note: The values shown are calculated surface strains at $3\theta_y$ in-plane hinge rotation demands (unless otherwise noted) before the application of OOP moment demands and the average values of the east and west flanges.
[a]Maximum value measured during ramp-down (RD) loading.
[b]No LVDT was used above the spliced region.

Table 4. Strain-based acceptance criteria

Surface compressive strains, ε_c	Strain limit, $\varepsilon_c/1.5$	Number of cycles	Damage state
0.0055[a]	0.0037	1	Strength loss prevention
0.0045	0.0030	2	—
0.004	0.0027	6	—
0.00375	0.0025	1	Damage prevention
0.0035	0.0023	10	—
0.003	0.0020	16	—
0.0025	0.0017	26	—

[a]This value was calculated using CW-2 LVDTs.

WLP was completed without any strength loss (IP or OOP) and the strain demands were higher compared with values for CW-3. The number of cycles was determined as the total number of cycles (including ramp-up and ramp-down) where the calculated compressive strain demands (at the base of the flange edges) were equal to or exceeded the values (ε_c) given in Table 4.

The recommended number of cycles at the specified strain limits in Table 4 are very conservative for the lower strain limits (lower-bound values) because significantly higher strain demands were applied to the specimens than the values given in Table 4. For example, the limit of 26 cycles at a compressive strain (ε_c) of 0.0025 is based on 10 cycles at 0.0025, 6 cycles at 0.003, 4 cycles at 0.0035, 4 cycles at 0.004, and 2 cycles at 0.0045; therefore, the actual number of cycles that could be applied prior to strength loss might be several (or many) times the values given in Table 4. The conservatism reduces as the magnitude of the strain increases in Table 4. Given the conservatism, these values are intended to provide guidance versus being hard limits. Results of analytical studies using calibrated nonlinear models might enable the development of more comprehensive and less conservative acceptance criteria and also consider a wider range of wall geometries, longitudinal reinforcement ratios, and axial load ratios.

In-Plane Lateral Stiffness for Linear Analysis

Based on the provisions of ACI 318-25 Appendix B, "Performance-Based Wind Design," the effective stiffness of concrete members can be calculated based on physical test data. For nonlinear analysis, comparisons of experimental and analytical results presented for load versus deformation responses indicate that moment-curvature analysis can reproduce the experimental results for the WLP, with possible adjustments for the effects of lap splices and slip/extension deformations. Prior studies for seismic tests (Orakcal and Wallace 2006; Gogus and Wallace 2015; Kolozvari et al. 2021) have reached similar conclusions. The use of beam-column elements with rigid plastic hinges is uncommon for nonlinear analysis of core walls because it is cumbersome; therefore, common engineering practice is to use strain-based acceptance criteria versus rotation-based acceptance criteria, e.g., for PBSD (LATBSDC 2023). However, linear analysis is common for lower intensity wind events, e.g., occupant comfort and operational performance objectives (ASCE 2019); therefore, effective in-plane flexural stiffness values (EI) of the C-shaped wall test specimens were calculated using Eq. (6), based on moment–rotation responses of the plastic hinge regions

$$EI = \frac{M_b L_p - \frac{1}{2} V_b L_p^2}{\theta_{\mathrm{LP,IP}}} \tag{6}$$

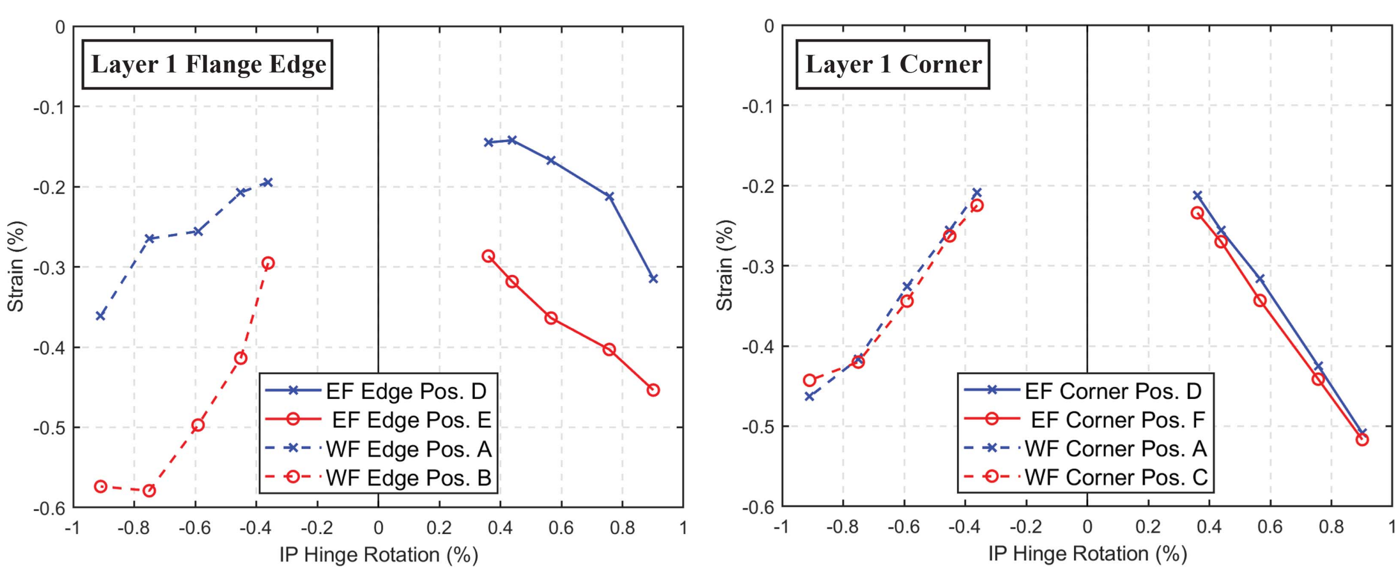

Fig. 22. Comparisons of CW-4 compressive LVDT strains at different loading positions during the ramp-up loading of WLP.

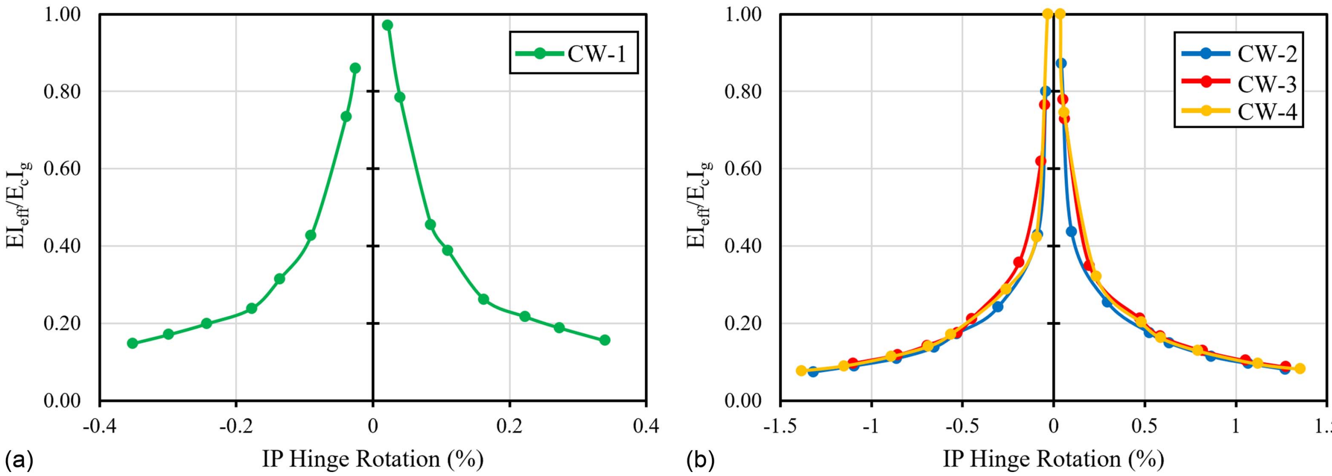

Fig. 23. Normalized effective flexural stiffnesses ($EI_{\text{eff}}/E_c I_g$).

where M_b and V_b = base moment and base shear, respectively; and $\theta_{\text{LP,IP}}$ = in-plane hinge rotation demand. EI values normalized to the concrete elastic modulus (E_c, calculated using Section 19.2.2.1 of ACI 318-25) times the gross section moment of inertia (I_g) are presented for different rotation demands. In Fig. 23, results are presented using $L_p = l_w/2 + L_s$ for the ramp-up portion of the WLP for CW-1 [Fig. 23(a)] and CW-2, CW-3, and CW-4 [Fig. 23(b)]. Accordingly, the EI values in Fig. 23 represent values for a wall with lap splices within the hinge region.

The results presented in Table 5 for uncracked (EI_{uncr}) and effective (EI_{eff}) flexural stiffness were calculated based on using a secant stiffness at cracking and first yield of the outer layer flange longitudinal reinforcement, respectively (Fig. 24). For the calculation of EI values in Table 5, two approaches were used: (1) including the splice region, $L_p = l_w/2 + L_s$ (to represent the average stiffness values of walls with lap splices within the hinge region), and (2) not including the splice region, i.e., based on $L_p = l_w/2$ above the splice region (to represent the stiffness values of a wall without lap splices within the hinge region). In addition, for each case, two approaches were used to calculate $\theta_{\text{LP,IP}}$: (1) including the rotations due to the slip/extension deformations that occurred at the wall–footing interfaces, and (2) excluding the slip/extension rotations, which were calculated using the LVDTs attached at the wall–foundation interface (at the four corners of the specimens).

The results presented in Table 5 indicate that, for linear analysis of walls with lap splices where slip/extension deformations are not modeled explicitly, $EI_{\text{eff}} = 0.3E_c I_g$ is recommended if the splice region is not modeled explicitly. On the other hand, if the lap splice region is modeled explicitly and slip/extension deformations are not modeled explicitly, $EI_{\text{eff}} = 0.8E_c I_g$ and $0.2E_c I_g$ are recommended for the lap splice region and for the regions above the splice, respectively. Alternative values are provided in Table 5 if the deformations due to slip/extension are modeled explicitly.

Table 5. Uncracked and cracked effective flexural stiffness values

Condition	ρ_l (%)	With lap splices EI_{uncr}	EI_{eff}	Without lap splices EI_{uncr}	EI_{eff}
With slip/extension deformations	0.75 1.5	$0.80E_c I_g$	$0.4E_c I_g$ $0.30E_c I_g$	$0.6E_c I_g$	$0.35E_c I_g$ $0.20E_c I_g$
Without slip/extension deformations	0.75 1.5	$1.0E_c I_g$	$0.70E_c I_g$ $0.40E_c I_g$	$1.0E_c I_g$	$0.65E_c I_g$ $0.30E_c I_g$

For walls with axial load demands different from $0.1A_g f_c'$, an evaluation of the test results indicates that moment-curvature analysis could be used to determine estimates of the flexural stiffness, with or without lap splices and either explicit modeling of slip/extension deformations or reducing EI to account for slip/extension deformations.

Summary and Conclusions

Four approximately one-third-scale C-shaped walls were tested in two phases to investigate the behavior of the ACI 318-25 ordinary reinforced concrete structural walls under wind loading protocols. For the Phase I walls, the longitudinal reinforcement ratio (ρ_l) was varied, i.e., 0.75% and 1.5% for CW-1 and CW-2, respectively. Phase II walls (CW-3 and CW-4) had the same cross-section dimensions as Phase I walls and the same amount of longitudinal reinforcement as CW-2 (1.5%). The test variables for CW-3 and CW-4 were the amount of confinement provided at the flange edges, i.e., hoops were used instead of U-bars, and the amount of axial load applied during the biaxial wind loading protocol, i.e., axial load was decreased to $0.05A_g f_c'$ and $0.075A_g f_c'$ for CW-3 and CW-4, respectively, during the biaxial loading (out-of-plane) to account for the variation in axial load due to the presence

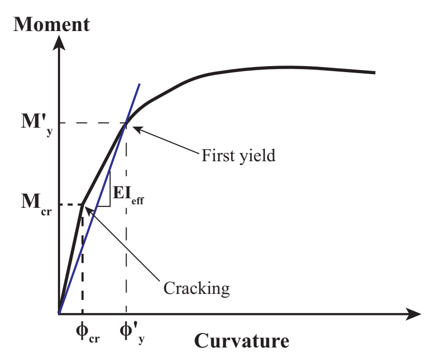

Fig. 24. Cracking and first yield of the walls.

of coupling beams. Based on the experimental results of the Phase I and Phase II tests, the following conclusions and recommendations are made:

- The wall with the lower longitudinal reinforcement ratio (CW-1) sustained no damage (e.g., concrete spalling, concrete crushing, rebar buckling, or rebar rupture) during the WLP. The residual flexural crack widths were very small (around 0.1 mm). This behavior suggests that moderate inelasticity during extreme wind events for ordinary walls with low-to-moderate longitudinal reinforcement ratios and axial stress levels will perform adequately without additional detailing requirements.
- The walls with higher longitudinal reinforcement ratios (CW-2, CW-3, and CW-4) had more damage compared with CW-1. For CW-2, the damage was significant at the base of the flange edges, i.e., for the east flange, approximately 23% of the total length of the flange sustained substantial concrete crushing at the base, and longitudinal bar buckling was observed above the footing–wall interface for the extreme layer flange edge longitudinal reinforcement.
- The variation of axial load during biaxial loading and the improved detailing at the flange edges resulted in less damage for Phase II walls, i.e., only cover spalling was observed at the base of the east flange edge for CW-3 ($P = 0.05A_g f'_c$), and cover spalling, longitudinal bar buckling and rupture of a single longitudinal bar at the base of the east flange edge were observed for CW-4 ($P = 0.075A_g f'_c$). The test results indicate that the design approach implemented was successful in limiting strength loss; however, additional modeling studies are needed to develop more comprehensive recommendations for required detailing for different wall geometries, material strengths, and reinforcement.
- The overlapping of longitudinal reinforcement, along with the tighter spacing of transverse reinforcement used, resulted in a stiffer and stronger splice region relative to the region immediately above the splice. Accordingly, the damage was concentrated primarily at the wall–footing interfaces and above the splice regions. The results presented indicate that increasing the assumed plastic hinge length by the splice length (i.e., $L_p = l_w/2 + L_s$) provided a simple and effective approach to estimate rotation demands. When $L_p = l_w/2 + L_s$ was used, the maximum rotational ductility values were 3.8, 4.2, and 4.9 for CW-2, CW-3, and CW-4, respectively, which exceeded the target acceptance criteria of 3.0 (as prescribed per the WLP).
- Given that the rotational ductility demands for the WLP reached 4.2 and 4.9 for CW-3 and CW-4, modest inelasticity can be allowed for the ordinary walls with higher longitudinal reinforcement ratios ($\rho_l = 1.5\%$) if the axial load demands during the biaxial loading when the flange edges are under compression is less than or equal to $0.075A_g f'_c$ and moderate confinement is provided at the flange edges. Volumetric transverse reinforcing ratios of 0.57% and 0.38% were provided for the flanges of the Phase II walls at the base of the walls and above the splice region, respectively, which are 2.33 times that required for ordinary walls (ACI 318-25, Chapter 11), but only 0.33 of that required for special walls (ACI 318-25, Chapter 18). Detailed analytical models that can accurately capture the concrete compressive strains could be used to predict the behavior of walls with different geometries, different reinforcing ratios, and higher axial loads.
- Strain-based acceptance criteria are recommended with peak compressive strain limits of 0.0025 (strain at peak unconfined stress) and 0.0037 for operational and continuous occupancy performance objectives of the ASCE prestandard for PBWD, respectively. In addition, lower compressive strain limits are provided based on the number of cycles at or below the given strain limit.
- Analytical predictions calculated using monotonic moment-curvature analysis results, calculated using the tested material (concrete and steel reinforcement) properties and assuming plane sections remain plane, resulted in a good match between the predicted and the experimental moment–hinge rotation and base shear–drift ratio responses in terms of stiffness (before and after concrete cracking) and maximum strength (e.g., M_n, M_{pr}, or $V_{@Mpr}$). The results indicated that the use of moment-curvature analysis, with appropriate consideration of the effects of the lap splice and the slip/extension deformations, produced reasonable estimates of flexural stiffness and *P-M* strength. More complex nonlinear models that are capable of predicting responses under biaxial loading histories were presented by Unal (2024) and will be the subject of a future paper (Unal and Wallace, "Nonlinear modeling of C-shaped reinforced concrete walls tested under wind and seismic loading protocols," submitted, *J. Struct. Eng.*, ASCE, Reston, Virginia).
- Based on the experimental results, different uncracked and cracked effective flexural stiffness values are recommended for linear analysis of walls under wind demands, depending on the existence of lap splices and explicit modeling of rotations/displacements due to slip/extension of longitudinal reinforcement.
- A secant-to-first yield shear stiffness value ranging from $0.02E_c$ to $0.1E_c$ can be used based on the experimental results and is similar to values proposed by PEER/ATC 72 and Kolozvari et al. (2021). Sensitivity studies are recommended for building analysis and design to assess the potential variation in predicted responses due to variations in shear stiffness.
- Based on a review of the beam test results, lap splice provisions of ACI 318-25 for ordinary walls were found to be inadequate to allow modest inelasticity under applied WLPs. No splice damage was observed in the test walls; therefore, the design approach used, i.e., to increase the splice length and to decrease the spacing of the transverse reinforcement provided over the splice length, was effective and is recommended. Additional beam splice testing has been conducted to develop more comprehensive splice design recommendations; this information will be the topic of a future paper.

Data Availability Statement

Some or all data, models, or code that support the findings of this study are available from the corresponding author upon reasonable request.

Acknowledgments

The research presented in this paper was supported by funding from Charles Pankow, American Concrete Institute, and Magnusson Klemencic Associates (MKA) Foundations. The project was administered by Charles Pankow Foundation as CPF Agreement RGA No. 01-21. The authors would like to thank the project advisory committee members, Thomas Sabol, Saman A. Abdullah, Kristijan Kolozvari, David Fields, Ian McFarlane, Sean Clifton, Brad Malmsten, and Viral Patel, for their valuable input. We would also like to express our gratitude for donations from Webcor Builders Inc., Pacific Steel Group (PGS), and CalPortland for materials and fabrication of the test specimens. We would also like to thank UCLA students Santiago Rodriguez, Samuel Halim, and Kenneth Leon for all their help with the testing program.

Author Contributions

Mehmet Emre Unal: Investigation; Methodology; Project administration; Supervision; Validation; Visualization; Writing – original draft; Writing – review and editing. Eric Ahlberg: Conceptualization; Methodology; Resources; Supervision; Writing – review and editing. Kevin Aswegan: Funding acquisition; Investigation; Methodology; Writing – review and editing. Juliana Rochester: Methodology; Writing – review and editing. Ron Klemencic: Funding acquisition; Investigation; Methodology; Project administration; Writing – review and editing. John W. Wallace: Funding acquisition; Investigation; Methodology; Project administration; Supervision; Writing – original draft; Writing – review and editing.

References

Abdullah, S. A., K. Aswegan, S. Jaberansari, R. Klemencic, and J. W. Wallace. 2020. "Performance of reinforced concrete coupling beams subjected to simulated wind loading." *ACI Struct. J.* 117 (3): 283–295. https://doi.org/10.14359/51724555.

Abdullah, S. A., K. Aswegan, R. Klemencic, and J. W. Wallace. 2021. "Performance of concrete coupling beams subjected to simulated wind loading protocols—Phase II." *ACI Struct. J.* 118 (3): 101–116. https://doi.org/10.14359/51729356.

Abdullah, S. A., K. Aswegan, R. Klemencic, and J. W. Wallace. 2022. "Seismic performance of concrete coupling beams subjected to prior nonlinear wind demands." *Eng. Struct.* 268 (Oct): 114790. https://doi.org/10.1016/j.engstruct.2022.114790.

Abdullah, S. A., and J. W. Wallace. 2019. "Drift capacity of reinforced concrete structural walls with special boundary elements." *ACI Struct. J.* 116 (1): 183–194. https://doi.org/10.14359/51710864.

ACI (American Concrete Institute). 2025. *Building code requirements for structural concrete (ACI 318-25) and commentary (ACI 318R-25)*. Farmington Hills, MI: ACI.

Alsiwat, J. M., and M. Saatcioglu. 1992. "Reinforcement anchorage slip under monotonic loading." *J. Struct. Eng.* 118 (9): 2421–2438. https://doi.org/10.1061/(ASCE)0733-9445(1992)118:9(2421).

ASCE. 2019. *Prestandard for performance-based wind design*. Reston, VA: ASCE. https://doi.org/10.1061/9780784482186.

ASCE. 2022. *Minimum design loads and associated criteria for buildings and other structures*. ASCE/SEI 7-22. Reston, VA: ASCE.

ASTM. 2022. *Standard specification for deformed and plain low-alloy steel bars for concrete reinforcement*. ASTM A706/A706M-22. West Conshohocken, PA: ASTM.

ASTM. 2023a. *Standard practice for making and curing concrete test specimens in the field*. ASTM C31/C31M-23. West Conshohocken, PA: ASTM.

ASTM. 2023b. *Standard test method for compressive strength of cylindrical concrete specimens*. ASTM C39/C39M-23. West Conshohocken, PA: ASTM.

Chang, G. A., and J. B. Mander. 1997. *Seismic energy based fatigue damage analysis of bridge columns: Part 1—Evaluation of seismic capacity.* Technical Rep. No. NCEER-94-0006. Buffalo, NY: State Univ. of New York.

Chou, T.-A., S. H. Lee, C. Chang, and T. H.-K. Kang. 2023. "Reinforced concrete coupling beams with different layouts under seismic and wind loads." *ACI Struct. J.* 120 (4): 165–178. https://doi.org/10.14359/51738743.

FEMA. 1997. *NEHRP guidelines for the seismic rehabilitation of buildings*. FEMA 273. Washington, DC: FEMA.

FEMA. 2023. *NEHRP recommended revisions to ASCE/SEI 41-17, seismic evaluation and retrofit of existing buildings.* FEMA P-2208. Washington, DC: FEMA.

Gogus, A., and J. W. Wallace. 2015. "Seismic safety evaluation of reinforced concrete walls through FEMA P695 methodology." *J. Struct. Eng.* 141 (10): 04015002. https://doi.org/10.1061/(ASCE)ST.1943-541X.0001221.

Halim, S. D. 2024. "Experimental study on lap splice nonlinear fatigue behavior under wind-loading protocol." Master of Science thesis, Dept. of Civil and Environmental Engineering, Univ. of California.

Hill, A., J. Forbes, and C. J. Motter. 2023. *Nonlinear wind design of steel reinforced concrete (SRC) coupling beams: Final report*. Rep. No. 06-19. Haymarket, VA: Charles Pankow Foundation.

Hilson, C., C. Segura, and J. W. Wallace. 2014. "Experimental study of longitudinal reinforcement buckling in reinforced concrete structural wall boundary elements." In *Proc., 10th US National Conf. on Earthquake Engineering: Frontiers of Earthquake Engineering*. Oakland, CA: Earthquake Engineering Research Institute.

Kent, D. C., and R. Park. 1971. "Flexural members with confined concrete." *J. Struct. Div.* 97 (7): 1969–1990. https://doi.org/10.1061/JSDEAG.0002957.

Klemencic, R., J. Hooper, R. Larsen, K. Aswegan, and J. Hasselbauer. 2019. "Performance-based wind design: The path forward." In *Proc. Annual Meeting of the Los Angeles Tall Buildings Structural Design Council*. Los Angeles: Los Angeles Tall Buildings Structural Design Council.

Kolozvari, K., M. F. Gullu, and K. Orakcal. 2022. "Finite element modeling of reinforced concrete walls under uni- and multi-directional loading using Opensees." *J. Earth. Eng.* 26 (12): 6524–6547. https://doi.org/10.1080/13632469.2021.1927893.

Kolozvari, K., K. Kalbasi, K. Orakcal, and J. W. Wallace. 2021. "Three-dimensional model for nonlinear analysis of slender flanged reinforced concrete walls." *J. Eng. Str.* 236 (Jun): 112105. https://doi.org/10.1016/j.engstruct.2021.112105.

LATBSDC (Los Angeles Tall Buildings Structural Design Council). 2005. *An alternative procedure for seismic analysis and design of tall buildings located in the Los Angeles region*. Los Angeles: LATBSDC.

LATBSDC (Los Angeles Tall Buildings Structural Design Council). 2023. *An alternative procedure for seismic analysis and design of tall buildings*. Los Angeles: LATBSDC.

Motter, C., S. Abdullah, and J. W. Wallace. 2018. "Reinforced concrete structural walls without special boundary elements." *ACI Struct. J.* 115 (3): 723–733. https://doi.org/10.14359/51702043.

Moyer, M. J., and M. J. Kowalsky. 2003. "Influence of tension strain on buckling of reinforcement in concrete columns." *ACI Struct. J.* 100 (1): 75–85. https://doi.org/10.14359/12441.

Orakcal, K., and J. W. Wallace. 2006. "Flexural modeling of reinforced concrete walls—Experimental verification." *ACI Struct. J.* 103 (2): 196–206. https://doi.org/10.14359/15177.

PEER and ATC (Pacific Earthquake Engineering Research Center and Applied Technology Council). 2010. *Modeling and acceptance criteria for seismic design and analysis of tall buildings*. PEER/ATC 72-1. Richmond, CA: PEER.

Rodriguez, M. E., J. C. Botero, and J. Villa. 1999. "Cyclic stress-strain behavior of reinforcing steel including effect of buckling." *J. Struct. Eng.* 125 (6): 605–612. https://doi.org/10.1061/(ASCE)0733-9445(1999)125:6(605).

Rodriguez, M. E., and M. Iñiguez. 2019. "Drift capacity at onset of bar buckling in RC members subjected to earthquakes." In *Proc., Concrete Structures in Earthquake*. Singapore: Springer. https://doi.org/10.1007/978-981-13-3278-4_12.

Segura, C. L., and J. W. Wallace. 2018. "Seismic performance limitations and detailing of slender reinforced concrete walls." *ACI Struct. J.* 115 (3): 849–859. https://doi.org/10.14359/51701918.

Thomsen, J. H., and J. W. Wallace. 2004. "Displacement-based design of slender reinforced concrete structural walls—Experimental verification." *J. Struct. Eng.* 130 (4): 618–630. https://doi.org/10.1061/(ASCE)0733-9445(2004)130:4(618).

Tura, C., K. Orakcal, M. F. Gullu, and A. Ilki. 2024. "Nonlinear modeling and response simulation of reinforced concrete walls under generalized loading conditions." In *Proc., 18th World Conf. on Earthquake Engineering*. Tokyo: International Association of Earthquake Engineering.

Unal, M. E. 2024. "Performance of ordinary C-shaped reinforced concrete structural walls subjected to wind and seismic loading protocols."

Ph.D. dissertation, Dept. of Civil and Environmental Engineering, Univ. of California.
Unal, M. E., J. W. Wallace, S. A. Abdullah, S. Kim, and K. Kolozvari. 2024. "Testing of lap splices in reinforced concrete beams and structural walls under wind loading protocols." In *Proc., 18th World Conf. on Earthquake Engineering*. Tokyo: International Association of Earthquake Engineering.
Wallace, J. W., and K. Orakcal. 2002. "ACI 318-99 provisions for seismic design of structural walls." *ACI Struct. J.* 99 (4): 499–508. https://doi.org/10.14359/12119.